Fabrication and Characterization of Silicon Compound Refractive Lenses for APS CHEX Beamline

Lisa M. Gades[1], Matthew J. Highland[1], Xianbo Shi[1], Matthew G. Frith[1], C. Suzanne Miller[2], Orlando Quaranta[1], Luca Rebuffi[1], and Brandon M. Stone[1]

[1]X-ray Sciences Division, Argonne National Laboratory, Lemont, IL 60439
[2]Nanosciences and Technology Division, Argonne National Laboratory, Lemont, IL 60439

Focusing of high-energy x-rays will be essential for beamlines redesigned to take advantage of the APS Upgrade, with its ultra-bright, high-coherence x-rays. While commercial compound refractive lenses (CRLs) are available in materials such as aluminum, beryllium, and nickel, they are expensive and often have a long lead-time. We have previously shown success with silicon (Si) CRLs for x-ray focusing of 106 keV x-rays for the SRS beamlines at APS Sector 11 [1]. For this project, we explored design solutions for the CHEX feature beamline at APS Sector 28 (Coherent High-Energy X-ray Sector for *In Situ* Science). Post APS-U CHEX will utilize the increased coherent flux at high energies for in-situ coherent scattering studies in complex environments such as materials synthesis and processing. Short arrays of parabolic lenses were fabricated via Deep Reactive Ion Etching (DRIE) at CNM and characterized at the IDEA beamline at APS Sector 28. We explored a selection of lens thicknesses (5, 10, 20 um), aperture sizes (230, 330 um), radii of curvature (Rc 30 vs. 50 um), etch depths (135, 200 um), and number of lenses (1, 3, 5, 8 lenses per array). Lens arrays were characterized at the IDEA beamline with measurements of Rc achieved, RMS wavefront error, yield, phase distortion, and radiography. The Rc of the etched lenses was close to the design (within 5%). We achieved good yield with a 10 um lens design (actual thickness ~7 um) to a depth of 200 um, an aspect ratio of ~30:1. This represents a lower bound for lens thickness, under the current etch recipe. In some cases, features in the characterization could be linked to the etch process. For example, each time the DRIE was stopped and restarted, a striation appeared in the etched sidewall. Results suggest that Si CRLs are a reasonable focusing option to pursue for the higher-energy CHEX branchlines, and this study was helpful in optimizing the lens designs for CHEX.

Use of the Center for Nanoscale Materials was supported by the U.S. Department of Energy, Office of Science, Office of Basic Energy Sciences, under Contract No. DE-AC02-06CH11357. Work at Argonne National Laboratory was supported by the U.S. Department of Energy, Office of Science, Office of Basic Energy Sciences, under Contract No. DE-AC02-06CH11357.

[1] Ruett, Uta, Gades, Lisa, Borkiewicz, Olaf, Quaranta, Orlando, Beyer, Kevin, Jennings, Guy, Suzanne Miller, C., and Miceli, Antonino. *Etched Silicon Planar CRL Optics for the High-Energy X-ray Diffraction Beamlines 11-ID-B and 11-ID-C at the APS*. United States: N. p., 2022. Web. doi:10.1088/1742-6596/2380/1/012060.

Fabrication And Characterization Of Silicon Compound Refractive Lenses For APS CHEX Beamline

Lisa Gades[1], Matthew J. Highland[1], Xianbo Shi[1], Matthew G. Frith[1], C. Suzanne Miller[2], Orlando Quaranta[1], Luca Rebuffi[1], Brandon M. Stone[1]
[1]X-ray Science Division - Argonne National Laboratory, [2]Center for Nanoscale Materials - Argonne National Laboratory

Focusing of high-energy X-rays will be essential for beamlines redesigned to take advantage of the APS Upgrade, with its ultra-bright, high-coherence X-rays. While commercial compound refractive lenses (CRLs) are available in materials such as aluminum, beryllium, and nickel, they are expensive and often have a long lead-time. We have previously shown success with silicon (Si) CRLs for X-ray focusing of 106 keV X-rays for the SRS beamlines at APS Sector 11 [1]. For this project, we explored design solutions for the CHEX feature beamline at APS Sector 28 (Coherent High-Energy X-ray Sector for In Situ Science). Post APS-U CHEX will utilize the increased coherent flux at high energies for in-situ coherent scattering studies in complex environments such as materials synthesis and processing. Short arrays of parabolic lenses were fabricated via Deep Reactive Ion Etching (DRIE) at CNM and characterized at the IDEA beamline at APS Sector 28. We explored a selection of lens thicknesses (5, 10, 20 μm), aperture sizes (230, 330 μm), radii of curvature (Rc 30 vs. 50 μm), etch depths (135, 200 μm), and number of lenses (1, 3, 5, 8 lenses per array). Lens arrays were characterized at the IDEA beamline with measurements of Rc achieved, RMS wavefront error, yield, phase distortion, and radiography. The Rc of the etched lenses was close to the design (within 5%). We achieved good yield with a 10 μm lens design (actual thickness ~7 μm) to a depth of 200 μm, an aspect ratio of ~30:1. This represents a lower bound for lens thickness, under the current etch recipe. In some cases, features in the characterization could be linked to the etch process. For example, each time the DRIE was stopped and restarted, a striation appeared in the etched sidewall. Results suggest that Si CRLs are a reasonable focusing option to pursue for the higher-energy CHEX branchlines, and this study was helpful in optimizing the lens designs for CHEX.

Motivation

Motivation: X-ray Focusing for CHEX Beamlines with Si CRLs Fabricated In-House

- Cost reduction for APS Upgrade project
- Feasible to do multiple tests
- No commercial lenses work well at 45 keV; Si CRLs to be tested
- Each lens array focuses in one dimension; <1 μm spot size
- Wavefront preservation for coherence measurements at high energies
- Enabling new science
  - In situ scattering studies in complex environments

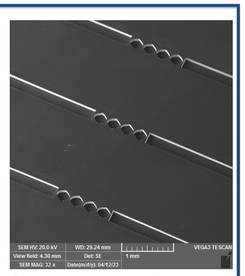

Short lens arrays for characterization at 20 keV

Fabrication

Design Specifications

- Silicon Prime wafers
- $R \approx 30$ and 50 μm
- Aperture ≈ 230 and 330 μm
- Lens thickness ≈ 5, 10, 20 μm
- Depth ≈ 136 and 200 μm
- Number of lenses: 1 – 8 per array
- Diced into square 10 mm chips

Process

- 6” Si Wafer
- Maskless Lithography: Heidelberg MLA-150, ~11 μm PR
- DRIE: Plasmatherm Versaline DSE
- Dicing: Thermocarbon Dicing Saw

Main Challenges

- Deep vertical sidewalls
- Reasonable etch rate
- Minimal overheating

Two Lenses with Aperture

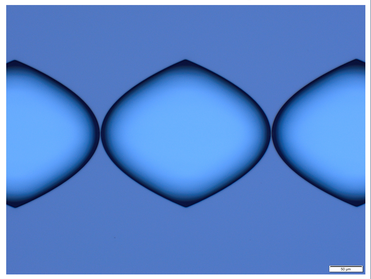

Characterization

Measurement Setup at the APS IDEA Beamline

- Methodology for typical 2D lens characterization can be applied to 1D Si etched CRLs
- Coded-mask-based at-wavelength X-ray metrology
- Spatial Resolution <1 μm and thickness error sensitivity to better than 0.1 μm
- Si Lenses measured at 20 keV
- Measuring 5 lenses at a time was the best mix of consistent results and good signal

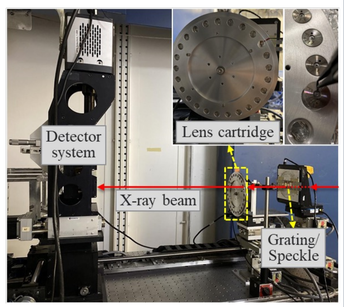

Lens measurement setup at the APS IDEA beamline (sector 28-ID-B)

Results

Results

- Lenses with thickness ≥ 10 μm worked consistently well
  - Actual thickness ~ 7 μm
  - Etched to 200 μm deep; **aspect ratio ~ 30:1**
- Lenses designed with 5 μm thickness were actually ~ 2.6 μm
  - Showed etch through with current DRIE process

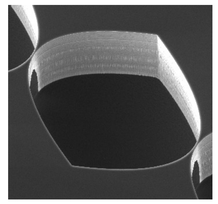

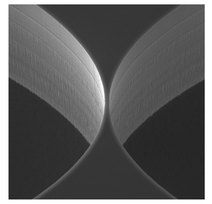

- Evidence of starting and stopping the DRIE process can be seen in horizontal stripes on the lens sidewalls
  - Stripes do not introduce a significant thickness error
- **See Table 1:** R = 30 μm: thicker wall tends to give smaller thickness error and less breakage (no trend at R = 50 μm)
- 5 x R30 lenses and 8 x R50 lenses give similar beam divergence, thus provide consistent radius results

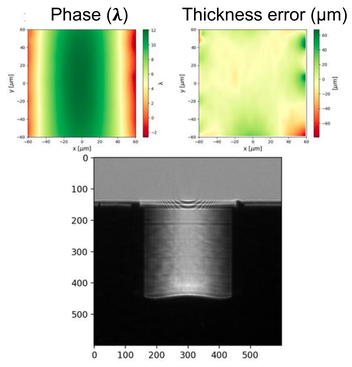

Typical results of 5 lenses, 10 μm thick

Table 1: Statistical Results	$\bar{R}$ (μm)	Total thickness RMS error, σ_T (μm)	Average single lens error, $\sigma_T/\sqrt{n}$ (μm)
R = 30 μm, T = 5 μm, n = 5	28.8	14.4	6.5
R = 30 μm, T = 10 μm, n = 5	29.0	12.4	5.5
R = 30 μm, T = 20 μm, n = 5	28.5	6.4	2.8
R = 50 μm, T = 5 μm, n = 8	47.7	12.5	4.4
R = 50 μm, T = 10 μm, n = 8	47.2	10.5	3.7
R = 50 μm, T = 20 μm, n = 8	47.6	14.0	4.9

Conclusion & Future Steps

Conclusion

- Etched Si Lenses are a via option for CHEX
  - Particularly on the highest energy G-branch

Future Steps

- Engineering a mounting scheme such that etched Si lenses can be easily mounted in CRL systems designed for traditional Be and Al lenses will facilitate their use.
- Test lenses at CHEX when APS Upgrade is complete
- Refine design and fabrication process as needed

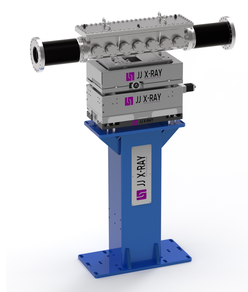

CRL System for CHEX high energy G-branch

References:

[1] Snigirev A, Snigireva I, Grigoriev M, Yunkin V, Di Michiel M, Kuznetsov S and Vaughan G (2007) "Silicon planar lenses for high-energy x-ray nanofocusing", Proc. SPIE6705 670506–11

[2] Stöhr, F. (2015). Microfabrication of hard x-ray lenses. Technical University of Denmark

[3] Ruett, Uta, Gades, Lisa, Borkiewicz, Olaf, Quaranta, Orlando, Beyer, Kevin, Jennings, Guy, Suzanne Miller, C., and Miceli, Antonino. *Etched Silicon Planar CRL Optics for the High-Energy X-ray Diffraction Beamlines 11-ID-B and 11-ID-C at the APS*. United States: N. p., 2022. Web. doi:10.1088/1742-6596/2380/1/012060.

Acknowledgements

Use of the Center for Nanoscale Materials was supported by the U.S. Department of Energy, Office of Science, Office of Basic Energy Sciences, under Contract No. DE-AC02-06CH11357. Work at Argonne National Laboratory was supported by the U.S. Department of Energy, Office of Science, Office of Basic Energy Sciences, under Contract No. DE-AC02-06CH11357.

April 19, 2023

Development of Dispersive X-ray Absorption Spectroscopy (XAS) on APS Beamline 25-ID

Juanjuan Huang[1], Adam Tornheim[2], George Sterbinsky[1]

[1]X-ray Science Division, Argonne National Laboratory, Lemont, IL 60439
[2]Chemical Sciences and Engineering Division, Argonne National Laboratory, Lemont, IL 60439

The beamline 25-ID at the Advanced Photon Source was recently commissioned with a newly designed monochromator, which allows switching between a Si(111) crystal pair and two sets of multilayer pairs. The double multilayer monochromators (DMM) have a bandwidth of a few percent, resulting in an increase of over an order of magnitude in the incident X-ray flux compared to silicon double crystal monochromators (DCM). The intense, polychromatic spectrum provided by the DMM is ideal for specific spectroscopic techniques such as dispersive X-ray absorption spectroscopy (DXAS). The key component of the dispersive setup is a polychromator, which disperses incident X-rays and forms an energy gradient due to a continuous variation of Bragg angles along the polychromator's curve surface. An area detector further resolves the spatially correlated energies, and absorption spectra can be generated after image processing. In comparison with conventional XAS, DXAS eliminates the need for scanning the monochromator and acquires a full spectrum in a single shot. This poster presents the current status of a DXAS development on beamline 25-ID, including instrument design, theoretical calculations, experimental characterization, and initial XAS results.

This research used resources of the Advanced Photon Source, a U.S. Department of Energy (DOE) Office of Science user facility and is based on work supported by Laboratory Directed Research and Development (LDRD) funding from Argonne National Laboratory, provided by the Director, Office of Science, of the U.S. DOE under Contract No. DE-AC02-06CH11357. Further, the authors would like to thank all staff of the APS Spectroscopy Group for their technical support.

DEVELOPMENT OF DISPERSIVE X-RAY ABSORPTION SPECTROSCOPY (DXAS) ON APS BEAMLINE 25-ID

Juanjuan Huang1, Adam Tornheim2, George E. Sterbinsky1
1 X-ray Science Division, Argonne National Laboratory, Lemont, IL 60439
2 Chemical Sciences and Engineering Division, Argonne National Laboratory, Lemont, IL 60439

ID25 BEAMLINE @ APS

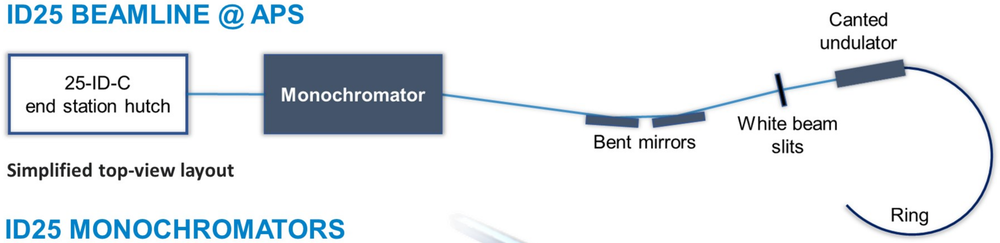

Simplified top-view layout

ID25 MONOCHROMATORS

Vertically deflecting LN2 cooled DCMs, switchable between

- Si (111) crystals
- B_4C/Mo multilayers (ML)
  - **ML 48 Å 5 – 10 keV (BW = 3%)**
  - **ML 24 Å 10 – 22 keV (BW = 1%)**

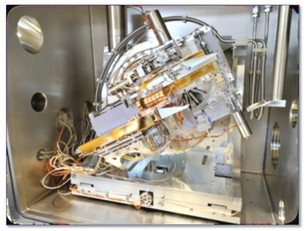

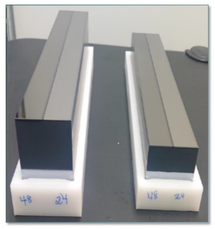

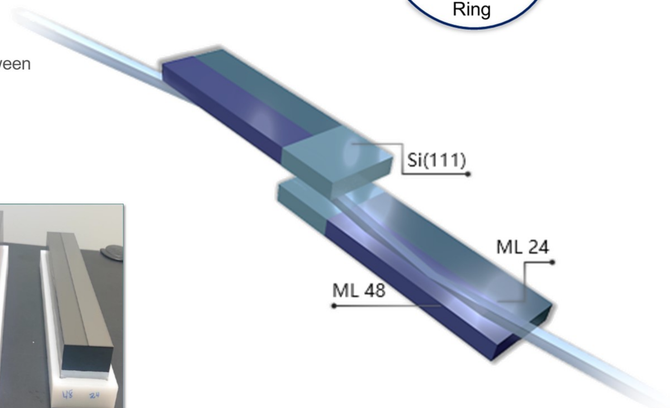

DISPERSIVE XAS SETUP @ 25-ID-C END STATION

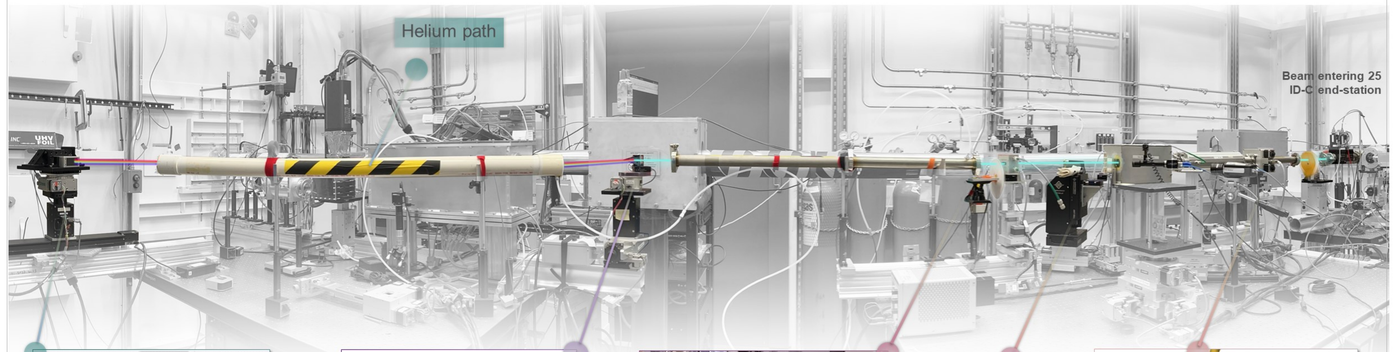

- Lambda 250 k photon-counting
- pixel size 55 µm
- FOV: 512 × 512 pixels

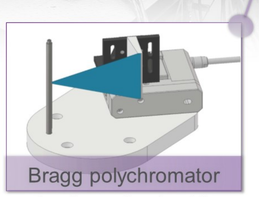

- Bending radius tunable
- Cylindrically bent

- reduce beam coherence
- reduce beam inhomogeneity
- reduce effects from sample inhomogeneity

Sample stage

- Nano positioner
- X-ray focal size on sample: ~ 1 µm

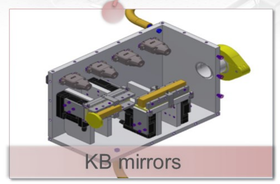

- Rh coated for lower energies
- Pt coated for higher energies

DXAS DATA ACQUISITION

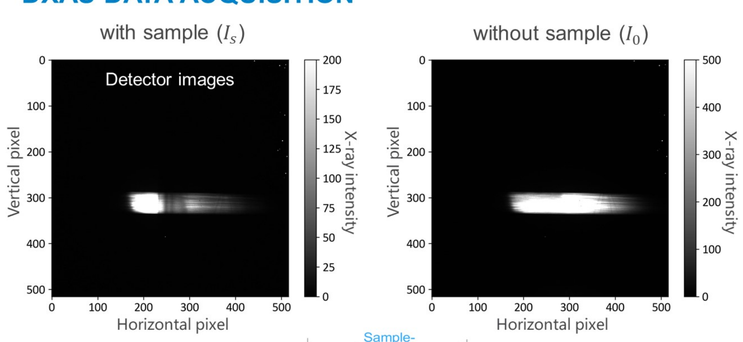

$$Abs = -log\left(\frac{I_s}{I_0}\right)$$

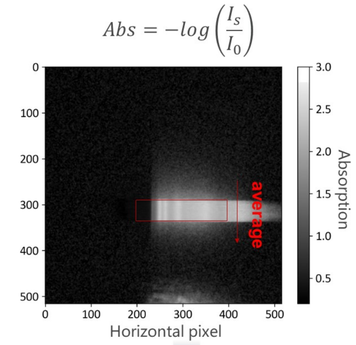

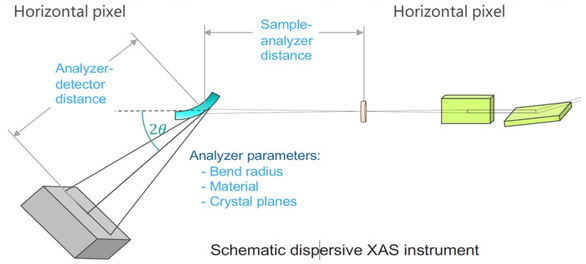

Schematic dispersive XAS instrument

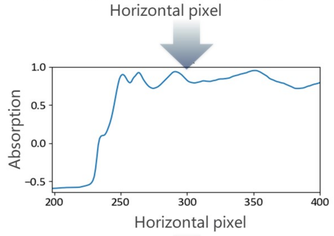

Polynomial fitting

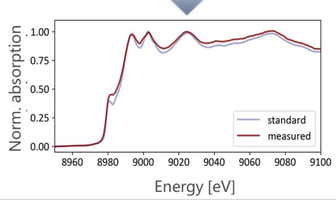

RESULTS Ni standards K-edge XANES

Compared with data measured by conventional double crystal monochromator @ 20 BM, APS

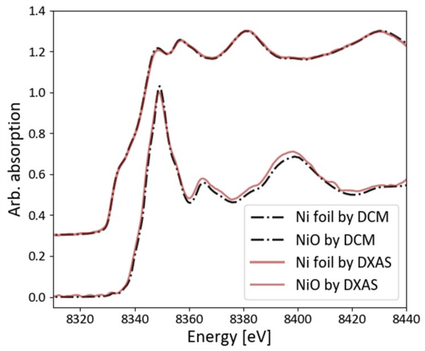

EX-SITU XANES Mn K-edge XANES

Mn-redox based cathode in different states of charges

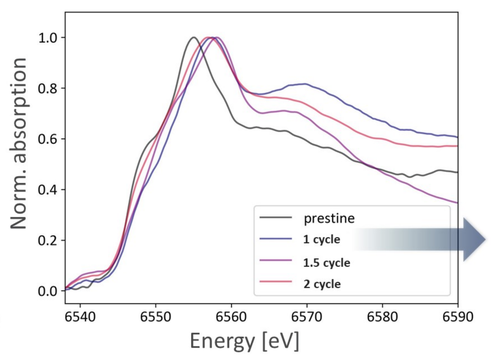

XANES MAPPING

The "1 cycle" sample was further mapped

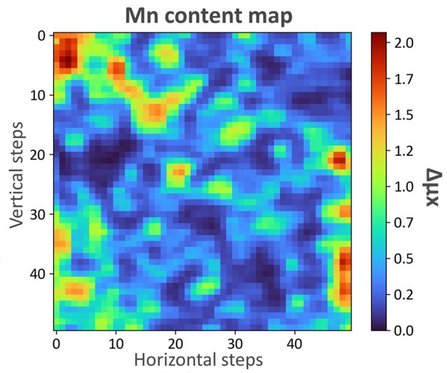

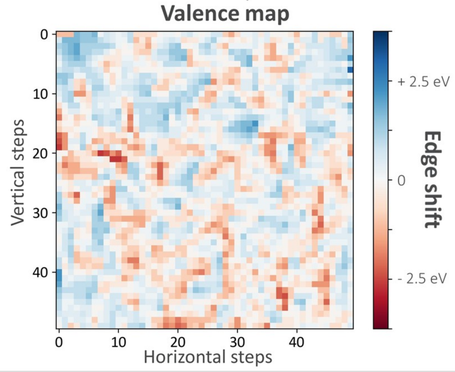

NEXT STEPS

- **Software development** for quick data preview/large dataset handling
- Continue **hardware development** for the final goal of *in-situ/operando* XANES mapping

- Numerical calculation studies, e.g., Si(111) @ 9 kV

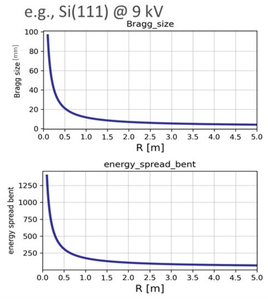

- Simulations e.g., ray tracing

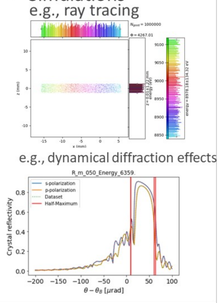

e.g., dynamical diffraction effects

ACKNOWLEDGEMENT

This research used resources of the Advanced Photon Source, a U.S. Department of Energy (DOE) Office of Science user facility and is based on work supported by Laboratory Directed Research and Development (LDRD) funding from Argonne National Laboratory, provided by the Director, Office of Science, of the U.S. DOE under Contract No. DE-AC02-06CH11357. Further, the authors would like to thank all staff of the APS Spectroscopy Group, in particular Shelly Kelly, Yanna Chen and Mark Wolfman for their technical & IT support, fruitful discussions.

Design, Fabrication, and Characterization of X-ray Optics for the Cavity-based X-ray Free-electron Laser Project

Peifan Liu[1], Paresh Chandra Pradhan[1], Xianbo Shi[1], Deming Shu[1], Keshab Kauchha[1], Zhi Qiao[1], Kenji Tamasaku[2], Taito Osaka[2], Diling Zhu[3], Xianrong Huang[1], Lahsen Assoufid[1], Marion White[1], Kwang-Je Kim[1], and Yuri Shvyd'ko[1]

[1]Advanced Photon Source, Argonne National Laboratory, Lemont, IL 60439
[2]RIKEN Spring-8 Center, 1-1-1 Kouto, Sayo-cho, Sayo-gun, Hyogo, 679-5148, Japan
[3]SLAC National Accelerator Laboratory, Menlo Park, CA 94025

A cavity-based x-ray free-electron laser (CBXFEL) is a possible future direction in the development of high-brilliance x-ray sources. CBXFELs consist of a low-emittance electron source, a magnet system with several undulators and chicanes, and an x-ray cavity. The x-ray cavity stores and circulates x-ray pulses for repeated FEL interactions with electron pulses until the FEL reaches saturation. CBXFEL cavities require low-loss wavefront-preserving components: near-100%-reflectivity x-ray diamond Bragg-reflecting crystals, outcoupling devices such as thin diamond membranes or x-ray gratings, and aberration-free focusing elements.

Here, we report on the design, manufacturing, and characterization of x-ray optical components for a CBXFEL x-ray cavity in a framework of a CBXFEL collaborative R&D project of Argonne National Laboratory, SLAC National Laboratory, and Spring-8. The cavity includes high-reflectivity diamond crystal mirrors with thin drumhead diamond membranes, Beryllium refractive lenses, and channel-cut Si monochromators. Diamond crystals with almost flawless 2×2 mm^2 regions of interest (ROI) were selected and furnished with strain-relief cuts for strain-free mounting. All crystals were characterized and exhibit small Bragg-plane slope errors of $\lesssim$ 0.2 μrad in the ROIs and small wavefront phase errors of $\lesssim \lambda/70$ on a footprint of 100 μm in diameter. In addition, diamond drumhead membranes with a thickness of < 20 μm were successfully manufactured. The Be lenses were characterized by x-ray phase-contrast imaging featuring wavefront errors $\lesssim \lambda/70$ on a footprint of 200 μm in diameter. Furthermore, 2-bounce and 4-bounce channel-cut Si monochromators have been successfully manufactured and tested to meet the desired performance and will be used as x-ray outcoupling monochromators to reduce the spontaneous radiation background and to single out x-rays with a small bandwidth in the peak of the cavity spectral distribution. These optical components are available to be installed in the CBXFEL cavity soon.

We are grateful to Michael Wojcik for support at the Advanced Photon Source 1BM beamline and Elina Kasman for polishing the Si channel-cut monochromators. Sergey Antipov is acknowledged for machining the diamond drumheads. Ryan Lindberg and Yuanshen Li at ANL, and Gabriel Marcus and Zhirong Huang at SLAC, are acknowledged for helpful discussions. Work at ANL is supported by the U.S. Department of Energy, Office of Science, Office of Basic Energy Sciences, under contract No. DE-AC02-06CH11357.

Design, Fabrication, and Characterization of X-Ray Optics for the Cavity-Based X-Ray Free-Electron Laser Project

Peifan Liu[1], Paresh Chandra Pradhan[1], Xianbo Shi[1], Deming Shu[1], Keshab Kauchha[1], Zhi Qiao[1], Kenji Tamasaku[2], Taito Osaka[2], Diling Zhu[3], Xianrong Huang[1], Lahsen Assoufid[1], Marion White[1], Kwang-Je Kim[1], Yuri Shvyd'ko[1,†]

[1] *Advanced Photon Source, Argonne National Laboratory, Lemont, Illinois 60439, USA*
[2] *RIKEN SPring-8 Center, 1-1-1 Kouto, Sayo-cho, Sayo-gun, Hyogo, 679-5148, Japan*
[3] *SLAC National Accelerator Laboratory, Menlo Park, CA 94025, USA*
[†] *Email: shvydko@anl.gov*

A cavity-based x-ray free-electron laser (CBXFEL) is a possible future direction in the development of high-brilliance X-ray sources. CBXFELs consist of a low-emittance electron source, a magnet system with several undulators and chicanes, and an x-ray cavity. The x-ray cavity stores and circulates x-ray pulses for repeated FEL interactions with electron pulses until the FEL reaches saturation. CBXFEL cavities require low-loss wavefront-preserving components: near-100%-reflectivity x-ray diamond Bragg-reflecting crystals, outcoupling devices such as thin diamond membranes or x-ray gratings, and aberration-free focusing elements. Here, we report on the design, manufacturing, and characterization of x-ray optical components for a CBXFEL x-ray cavity in a framework of a CBXFEL collaborative R&D project of Argonne National Laboratory, SLAC National Laboratory, and Spring-8. The cavity includes high-reflectivity diamond crystal mirrors with thin drumhead diamond membranes, Beryllium refractive lenses, and channel-cut Si monochromators. Diamond crystals with almost flawless 2×2 mm^2 regions of interest (ROI) were selected and furnished with strain-relief cuts for strain-free mounting. All crystals were characterized and exhibit small Bragg-plane slope errors of $\lesssim$ 0.2 μrad in the ROIs and small wavefront phase errors of $\lesssim \lambda/70$ on a footprint of 100 μm in diameter. In addition, diamond drumhead membranes with a thickness of < 20 μm were successfully manufactured. The Be lenses were characterized by x-ray phase-contrast imaging featuring wavefront errors $\lesssim \lambda/70$ on a footprint of 200 μm in diameter. Furthermore, 2-bounce and 4-bounce channel-cut Si monochromators have been successfully manufactured and tested to meet the desired performance and will be used as x-ray outcoupling monochromators to reduce the spontaneous radiation background and to single out x-rays with a small bandwidth in the peak of the cavity spectral distribution. These optical components are available to be installed in the CBXFEL cavity soon.

Experimental setup for the Cavity-Based Free-Electron Laser (CBXFEL) project

G. Marcus, et al. *39th Free Electron Laser Conf./FEL2019, Hamburg, Germany*. 2019.

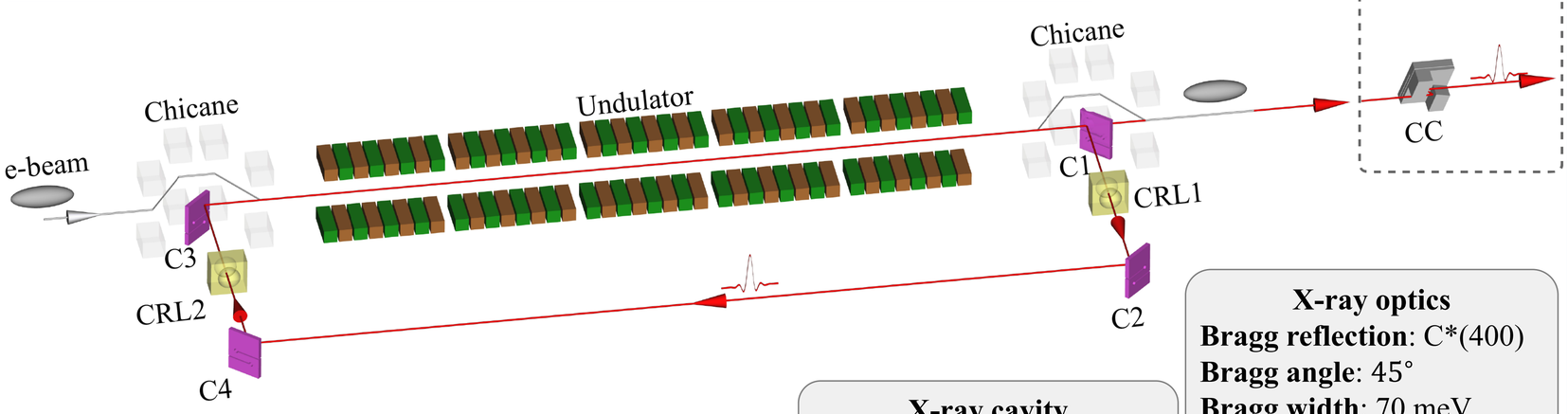

E-beam
Energy: 10.3 GeV
Bunch length: ~ 15 – 300 fs (4.5 – 90 μm)
RMS beam size: 22 – 24 μm
2-bunch separation: ~ 220 ns

X-ray
Energy: 9.831 keV
Pulse length: ~ 25 fs – 1 ps (7.5 – 300 μm)
Waist size: ~ 30 μm
Rayleigh range: ~ 28 m

X-ray cavity
4× diamond crystal mirrors, 2× Be CRL lenses
Roundtrip length: ~ 66 m (~ 220 ns)
Long-arm length: ~ 32 m
Short-arm length: ~ 0.65 m

X-ray optics
Bragg reflection: C*(400)
Bragg angle: 45°
Bragg width: 70 meV
C1: ~ 15 μm thick, output coupler
C2-C4: ~ 500 μm thick
All crystal temperature: < 1 K difference
Be lens: 28.3 m focal length

Project goals:

- 2-pass FEL gain measurement in both low-gain XFELO mode and high-gain XRAFEL mode
- X-ray cavity quality and cavity ring-down measurements

High-reflectivity diamond crystal mirrors

The low-loss x-ray cavity requires crystal mirrors with:

- high ≃ 98% x-ray Bragg reflectivity at (100) orientation with a small Bragg-plane miscut angle
- small Bragg-plane slope errors $\lesssim$ 0.2 μrad/mm^2 (rms) [$\frac{1}{10}$th of the XFEL beam rms angular divergence]
- small wavefront phase errors over 100×100 μm^2

Machining of Sumitomo diamond HPHT (100) crystals (acquired by SPring-8)

as-grown plate → ready for machining → machined by laser cutting → machined by laser ablation

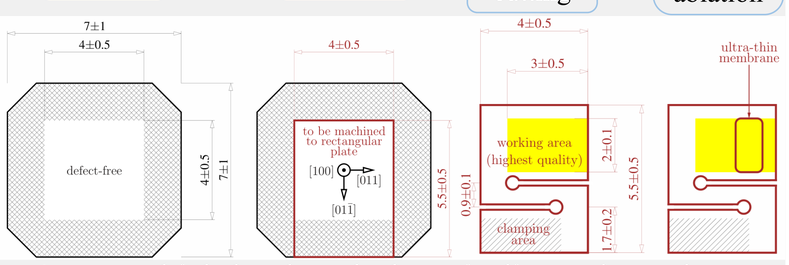

- From multiple batches, the best six diamond samples have been selected based on x-ray topography screening. They were then sent for laser cutting and annealed and screened again.

Example: Sumitomo DIa121 (546 μm thick) front surface

Crystal photograph | FWHM map | Center of mass map

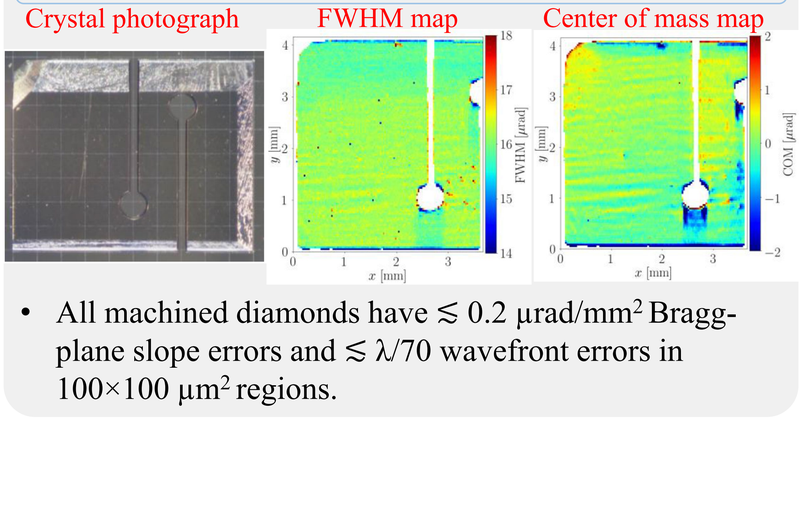

- All machined diamonds have $\lesssim$ 0.2 μrad/mm^2 Bragg-plane slope errors and $\lesssim \lambda/70$ wavefront errors in 100×100 μm^2 regions.

Diamond drumhead crystal for outcoupling

Outcoupling of x-rays requires a thin-film diamond single crystal with ~10s microns thickness. Drumhead crystals are a solution ensuring mechanically stable strain-free mounting of the membranes with efficient thermal transport.

Crystal photograph | Microscope image | Rocking curve and thickness fitting

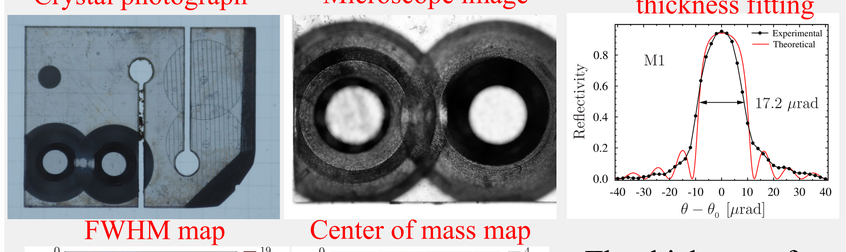

FWHM map | Center of mass map

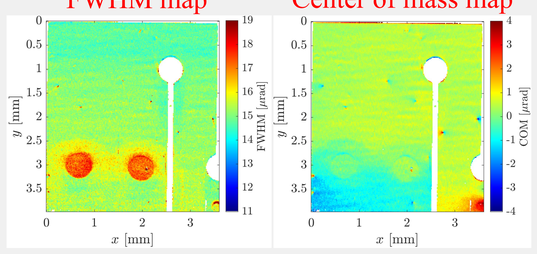

- The thickness of both membrane is ~16 μm.
- In a 2×2 mm^2 ROI, RMS COM is 0.24 μrad.

P. Pradhan, S. Antipov, and Yu. Shvyd'ko. *Advances in X-Ray/EUV Optics and Components XVII*. Vol. 12240. SPIE, 2022.

Beryllium refractive paraboloids lens

Beryllium paraboloidal lenses with radius of curvature R = 200 μm (f = 28.3 m) manufactured from IS50-M (smallest SAXS) and O30-H Be materials were obtained from RXOPTICS.

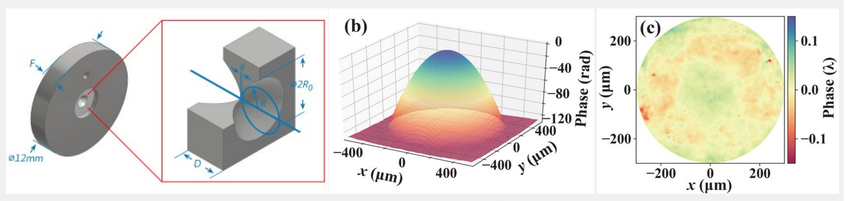

www.rxoptics.de/products/lenses/ Qiao, Zhi, et al. *Applied Physics Letters* 119.1 (2021): 011105.

- Differential thickness profiles of Beryllium O30-H lenses reveal less voids and shape errors than in the IS50-M lenses.
- The best lenses feature appropriate for CBXFEL quality with RMS residual error σ = 0.5 μm (D = 600 μm) and RMS phase error of $\leq \lambda/70$.

Si channel-cut crystal monochromators (for outcoupled x-ray)

Spontaneous radiation bandwidth of the CBXFEL undulator is ≃ 100 eV, i.e., > 10^3 broader than the 70-meV cavity bandwidth.

- A ≃ 60-meV bandwidth monochromator is required to reject the huge spontaneous radiation background [realized by using Si(620) Bragg reflections].
- A ≃ 20-meV bandwidth monochromator is required for clean measurements of the cavity ring-down [realized by using Si(660) Bragg reflections].
- Four-bounce channel-cut monochromators are required to better reject the background.

4×Si(620) channel-cut | 4×Si(660) channel-cut

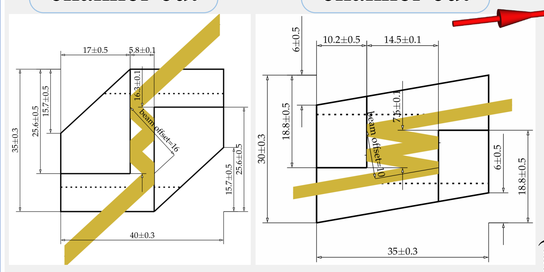

Bragg's angle θ = 47.250° (@9.831 keV) $\Delta\theta$ = 7.8 μm, ΔE = 71 meV

Bragg's angle θ = 80.126° (@9.831 keV) $\Delta\theta$ = 13.6 μm ΔE = 23 meV

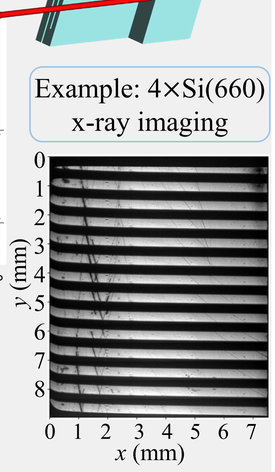

- The whole crystals are examined by vertically scanning the x-ray.
- All crystals are good in the 1st approximation.

Conclusion

- All cavity optical elements have been specified, designed, manufactured, and fully characterized.
- High-reflectivity strain-free-mounted diamond crystal mirrors were fabricated and fully characterized. All crystals have slope errors $\lesssim$ 0.2 μrad/mm^2 and wavefront errors $\lesssim \lambda/70$ on a footprint of 100 μm in diameter.
- Strain-free diamond drumhead crystals have been successfully manufactured with ~16 μm-thickness and 0.2 μrad Bragg-plane slope error.
- Paraboloidal Be lenses were acquired and characterized with x-ray phase-contrast imaging featuring small wavefront errors ($\lesssim \lambda/70$ on a footprint of 200 μm in diameter).
- Si channel-cut crystals for outcoupled x-rays were designed, manufactured, and characterized. They work well in the 1st approximation.

Acknowledgment

We are grateful to Michael Wojcik for support at the Advanced Photon Source 1BM beamline and Elina Kasman for polishing the Si channel-cut monochromators. Sergey Antipov is acknowledged for machining the diamond drumheads. Ryan Lindberg and Yuanshen Li at ANL, and Gabriel Marcus and Zhirong Huang at SLAC, are acknowledged for helpful discussions. Work at ANL is supported by the U.S. Department of Energy, Office of Science, Office of Basic Energy Sciences, under contract No. DE-AC02-06CH11357.

Hybrid Pixel Array Detector for Time-resolved and Imaging Applications with 56,000 fps Sustainable Frame Rate

Yasukazu Nakaye[1*], Yasutaka Sakuma[2], Satoshi Mikusu[2], and Takuto Sakumura[2]

[1]Rigaku Americas Corporation, The Woodlands, TX 77381
[2]Rigaku Corporation, Tokyo 196-8666, Japan

It has been more than ten years since HPAD (Hybrid Pixel Array Detectors) had been widely utilized as x-ray diffraction and imaging detectors. Thanks to its single photon counting capability, HPAD shows images without background noise and wide dynamic range. Due to limitations of the fabrication process, most HPADs are made with monolithic sensor and tiled readout ICs. In conventional HPAD, there were so-called “inter-chip pixels” on the edges of readout ICs. These inter-chip pixels have 1.5 times or wider width and/or height than non-inter-chip pixels. This means, we are losing position information of a hit of photons on those pixels. We have successfully dealt with this inter-chip pixel problem by use of re-distribution layer on the Silicon sensor. So, in our new detector, non-uniformity in a single sensor module is eliminated.

This new detector is designed based on UFXC32k IC [1] designed by AGH University of Science and Technology and named XSPA-500k [2]. XSPA-500k detector consists of 16 UHXC chips tiled and 1024 x 512 76 um sq. pixels per module. No inter-chip pixels in between ROICs which terribly suffer the image quality.

XSPA-500k is aiming not only for x-ray imaging but also for time-resolved x-ray measurements. Dealing with “inter-chip pixels” is our main feature for imaging, and for time-resolved measurements we understand that frame rate is as important as the size of the pixels and the area of the detector. Thanks to UFXC32k IC’s high count-rate and fast operation capability, combined with our high data throughput backend circuits, XSPA-500k is capable of up to 56,000 fps with full-frame readout and 100,000 fps with 100 lines ROI in the center of the modules with continuous exposure (zero-deadtime mode operation with 2-bit counter/pixel.) If the non-continuous exposure (burst-mode operation [3]) is allowed, it can achieve over 970,000 fps with approximately 2 % duty ratio.

[1] P. Grybos et al., “32k Channel Readout IC for Single Photon Counting Pixel Detectors with 75 μm Pitch, Dead Time of 85 ns, 9 e^-rms Offset Spread and 2% rms Gain Spread,” *IEEE Trans. Nucl. Sci.*, vol. 63, no. 2, pp. 1155-1161, Apr. 2016. DOI: 10.1109/TNS.2016.2523260 [Online] Available: https://ieeexplore.ieee.org/document/7454876.
[2] Y. Nakaye, et al., “Characterization and performance evaluation of the XSPA-500k detector using synchrotron radiation,” *J. Synchrotron Rad.* vol. 28, pp. 439-447, Mar. 2021. DOI: 10.1107/S1600577520016665 [Online] Available: https://scripts.iucr.org/cgi-bin/paper?S1600577520016665
[3] Q. Zhang et al., “Sub-microsecond-resolved multi-speckle X-ray photon correlation spectroscopy with a pixel array detector,” *J. Synchrotron Rad.*, vol. 25, pp. 1408-1416, Jun. 2018. DOI: 10.1107/S1600577518009074 [Online] Available: http://scripts.iucr.org/cgi-bin/paper?S1600577518009074

Design and Characterization of X-ray Diagnostics for the Cavity-based X-ray Free-electron Laser Project

Peifan Liu[1], Paresh Chandra Pradhan[1], Antonino Miceli[1], Donald A. Walko[1], Deming Shu[1], Joseph Sullivan[1], Keenan Lang[1], Mark Rivers[2], Diling Zhu[3], and Yuri Shvyd'ko[1]

[1]Advanced Photon Source, Argonne National Laboratory, Lemont, IL 60439
[2]Center for Advanced Radiation Sources, The University of Chicago, Lemont, IL 60439
[3]SLAC National Accelerator Laboratory, Menlo Park, CA 94025

A cavity-based x-ray free-electron laser (CBXFEL) is a possible future direction in the development of high-brilliance x-ray sources. CBXFELs are built upon repetitive FEL interactions between electron pulses in an undulator and circulating x-ray pulses in an x-ray cavity, consisting of near-100%-reflectivity x-ray Bragg-reflecting diamond crystal mirrors and aberration-free focusing elements. All cavity optical components have to be aligned with a precision ensuring that the to-be-amplified x-ray beam returning into the undulator (after traveling tens to hundreds of meters in the cavity and being refocused to a spot of a few tens of microns) meets a fresh electron bunch of a similar size and a few tens of microns in length.

Here, we report on the design, manufacturing, and evaluation of x-ray diagnostics components for the precise CBXFEL x-ray cavity alignment and characterization performed in a framework of a CBXFEL R&D collaborative project of Argonne National Laboratory, SLAC National Laboratory, and Spring-8. The CBXFEL x-ray diagnostics include x-ray beam position and profile monitors (XBPMs), x-ray beam intensity monitors (XBIMs), and a meV-resolution x-ray spectrograph. Four types of XBPMs are used to monitor the beam position and profile along the entire cavity: coarse-alignment photo-luminescent YAG XBPMs, fine-alignment photo-luminescent minimally-invasive diamond XBPM, x-ray microscopes to monitor x-ray beams on the diamond crystal mirrors, and fast electronic quadrant diamond XBPM. To measure x-ray photon intensity in individual x-ray pulses, both ns-resolution Si-based XBIMs extra-cavity (behind diamond mirrors), and intra-cavity ns-resolution minimally invasive diamond XBIM are used. All the diagnostics have been tested and calibrated with pulsed x-rays at Advanced Photon Source (APS) beamlines 1-BM-B, 4-ID-D, and 7-ID-B. These diagnostics components will be installed inside or outside the FEL cavity to ensure the accuracy of the initial beam alignment, final fine beam alignment, and to characterize and optimize FEL performance.

We are grateful to Michael Wojcik, Alan Kastengren, Troy Lutes, Jeff Hoffman, Mark Engbretson, Keshab Kauchha, and Daniel Haskel for support with experiments at APS beamlines 1BM, 4ID, and 7ID. Kwang-Je Kim, Marion White, Ryan Lindberg (ANL), Zhirong Huang, Gabriel Marcus, and Alex Halavanau (SLAC) are acknowledged for helpful discussions. Work at ANL is supported by the U.S. Department of Energy, Office of Science, Office of Basic Energy Sciences, under contract No. DE-AC02-06CH11357.

Design and Characterization of X-Ray Diagnostics for the Cavity-Based X-Ray Free-Electron Laser Project

Peifan Liu[1], Paresh Chandra Pradhan[1], Antonino Miceli[1], Donald A. Walko[1], Deming Shu[1], Joseph Sullivan[1], Keenan Lang[1], Mark Rivers[2], Diling Zhu[3], Yuri Shvyd'ko[1,†]

[1] *Advanced Photon Source, Argonne National Laboratory, Lemont, Illinois 60439, USA*
[2] *Center for Advanced Radiation Sources, The University of Chicago, Argonne, Illinois 60439, USA*
[3] *SLAC National Accelerator Laboratory, Menlo Park, CA 94025, USA*
[†] *Email: shvydko@anl.gov*

A cavity-based x-ray free-electron laser (CBXFEL) is a possible future direction in the development of high-brilliance X-ray sources. CBXFELs are built upon repetitive FEL interactions between electron pulses in an undulator and circulating x-ray pulses in an x-ray cavity, consisting of near-100%-reflectivity x-ray Bragg-reflecting diamond crystal mirrors and aberration-free focusing elements. All cavity optical components have to be aligned with a precision ensuring that the to-be-amplified x-ray beam returning into the undulator (after traveling tens to hundreds of meters in the cavity and being refocused to a spot of a few tens of microns) meets a fresh electron bunch of a similar size and a few tens of microns in length. Here, we report on the design, manufacturing, and evaluation of x-ray diagnostics components for the precise CBXFEL x-ray cavity alignment and characterization performed in a framework of a CBXFEL R&D collaborative project of Argonne National Laboratory, SLAC National Laboratory, and Spring-8. The CBXFEL x-ray diagnostics include x-ray beam position and profile monitors (XBPMs), x-ray beam intensity monitors (XBIMs), and a meV-resolution x-ray spectrograph. Four types of XBPMs are used to monitor the beam position and profile along the entire cavity: coarse-alignment photo-luminescent YAG XBPMs, fine-alignment photo-luminescent minimally-invasive diamond XBPM, x-ray microscopes to monitor x-ray beams on the diamond crystal mirrors, and fast electronic quadrant diamond XBPM. To measure x-ray photon intensity in individual x-ray pulses, both ns-resolution Si-based XBIMs extra-cavity (behind diamond mirrors), and intra-cavity ns-resolution minimally invasive diamond XBIM are used. All the diagnostics have been tested and calibrated with pulsed x-rays at Advanced Photon Source (APS) beamlines 1-BM-B, 4-ID-D, and 7-ID-B. These diagnostics components will be installed inside or outside the FEL cavity to ensure the accuracy of the initial beam alignment, final fine beam alignment, and to characterize and optimize FEL performance.

Diagnostics overview for the Cavity-Based Free-Electron Laser (CBXFEL) project

G. Marcus, et al. *39th Free Electron Laser Conf./FEL2019, Hamburg, Germany*. 2019.

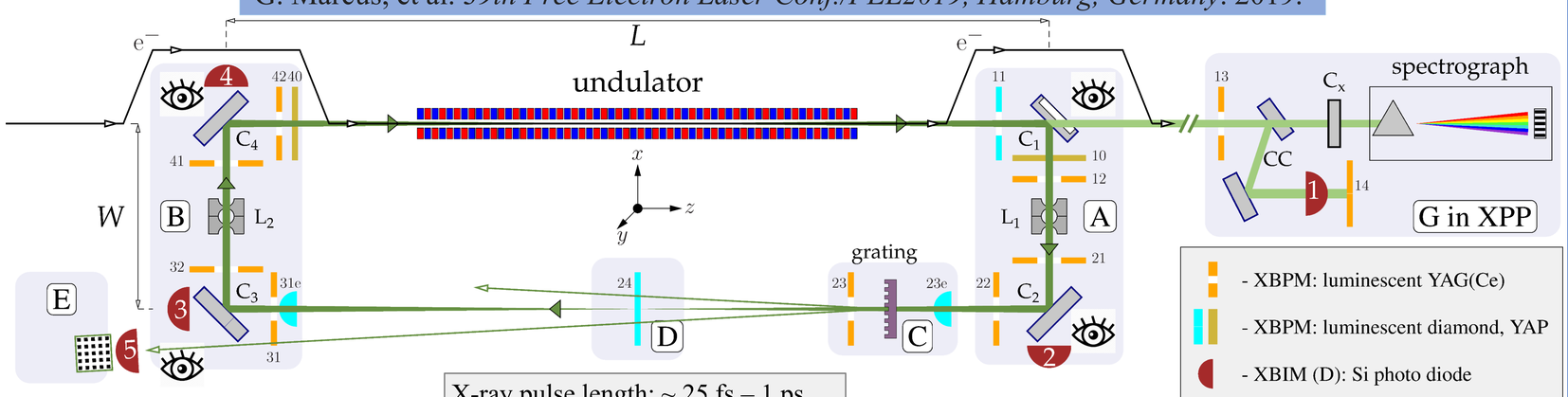

E-beam bunch length: ~ 15 – 300 fs (4.5 – 90 μm)
RMS e-beam size: 22 – 24 μm
2-bunch separation: ~ 220 ns

X-ray pulse length: ~ 25 fs – 1 ps (7.5 – 300 μm)
X-ray waist size: ~ 30 μm
Roundtrip length: ~ 66 m (~220 ns)
Long-arm length *L*: ~ 32 m

Cavity mirror: C*(400)
Bragg angle: 45°
Photon energy: 9.831 keV
Bragg width: 70 meV

The diagnostics include: 1) x-ray beam position monitors (XBPMs); 2) x-ray beam-intensity monitors (XBIMs); 3) a meV-resolution spectrograph. These diagnostics are designed assuming photon fluxes in the table below:

	Unit	XFELO		XRAFEL	
		1st pulse	2nd pulse	1st pulse	2nd pulse
Pulse flux total	[ph/pulse]	5×10^7	5×10^7	2×10^8	2.2×10^8
Pulse flux monochromatic	[ph/pulse/100 meV]	5×10^4	1×10^5	3.2×10^5	1.2×10^7
Average flux total	[ph/s]	6×10^9	6×10^7	2.4×10^{10}	2.6×10^{10}
Average flux monochromatic	[ph/s/100 meV]	6×10^6	1.2×10^7	3.8×10^7	1.4×10^9

Calculation: K.J. Kim, G. Marcus (2020)

ns-Resolution Si x-ray BIMs

- D1-D4 are critical for both initial and final alignment of the cavity; and measuring cavity ring-down and gain.
- Si diode (SM05PD1A) signal is digitized using 14-bit digitizer (Teledyne ADQ14).
- The smallest detectable signal is ~10 ph/pulse, and the dynamic range is $10 - 10^7$ ph/pulse (can go up).

SM05PD1A & ADQ14 digitizer

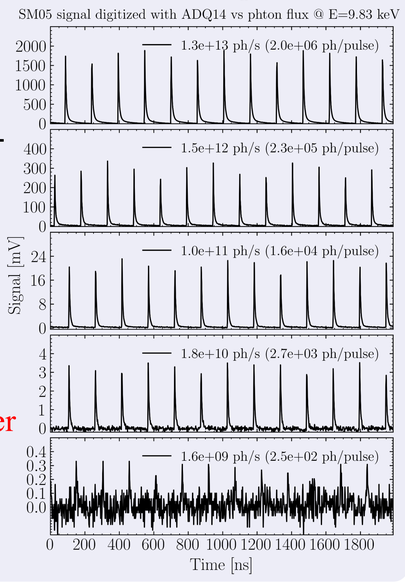

ns-Resolution diamond x-ray BIMs

X23e (Sydor-102) provides beam intensity information at the equivilent undulator center.

- The 45-μm-thick diamond sensor has low absorption (~5%).
- The smallest detectable signal is ~10^3 ph/pulse, and the dynamic range is $10^3 - 10^7$ ph/pulse (can go up).

X23e (Sydor 102)

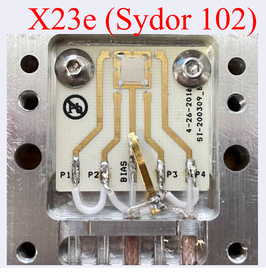

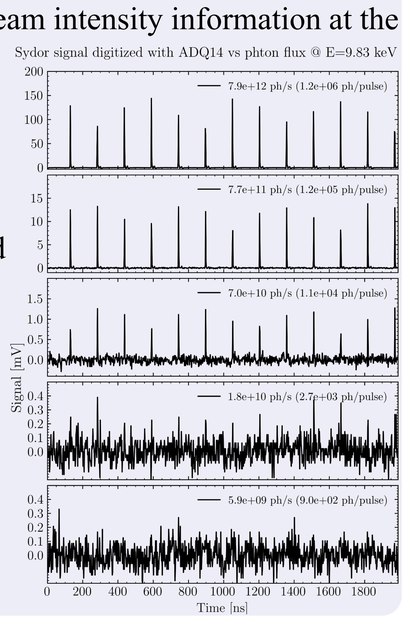

Luminescent XBPMs for coarse alignment

- They work under low flux ($10^5 - 10^7$ ph/s) with resolution < 10 μm.
- The camera (Prosilica) and optics (Infinity VideoMax) have long working distance (~180 mm) and large field of view (>10 × 10 mm²).
- 100-μm-thick YAG scintillators with 45° alignment holes (250-μm-aperture) and elliptical markings (repeating every 0.5 mm along minor axis) are used in all cases except 11, 13, and 24.
- X11 is downstream the undulator and sees a large synchrotron radiation background, a 30-μm-thick holed Diamond:B screen is used with the same camera and optics.

Camera & optics

YAG scintillator

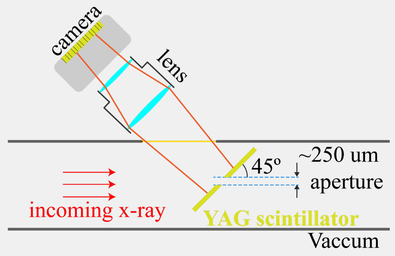

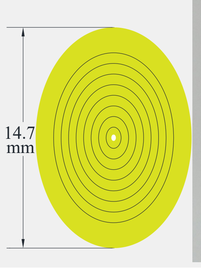

Minimally-invasive luminescent XBPM24 for fine alignment

- For fine alignment and live monitoring the beam position, a 30-μm-thick Diamond:B scintillator in XBPM24 is used.
- The scintillator signal is ~10 weaker than that from YAG, lower-noise camera (Andor Zyla) and large-NA optics (Infinity DistaMax) are used. Working distance is ~95 mm with resolution < 5 μm.
- X13 uses the same camera and optics, but with YAG screen with a ϕ1-mm hole.

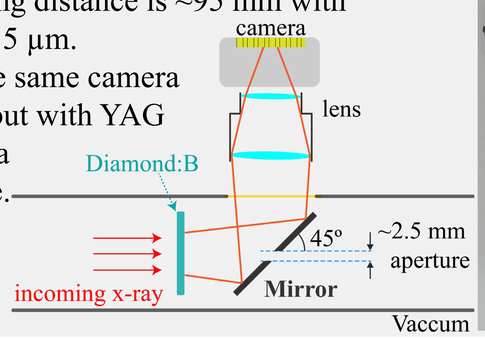

Camera & optics

Diamond electronic quadrant XBPM 31e

- Diamond XBMP X31e (Sydor DBPM-405V) is a minimally-invasive device transmitting 97% of 9.8-keV x-rays.
- Sensitive to CBXFEL beams with the flux as low as 10^6 ph/s expected in the cavity.
- Beam position sensitivity:
  ≲ 40 nm (rms) for a 10^7-ph/s x-ray beam;
  ≲ 1 μm (rms) for a 10^6-ph/s x-ray beam.
- Angular sensitivity:
  ≃ 1 nrad (rms) @ 10^7 ph/s;
  ≃ 30 nrad (rms) @ 10^6-ph/s (assuming 32-m distance from C2 to C3).

X31e test at 1BM

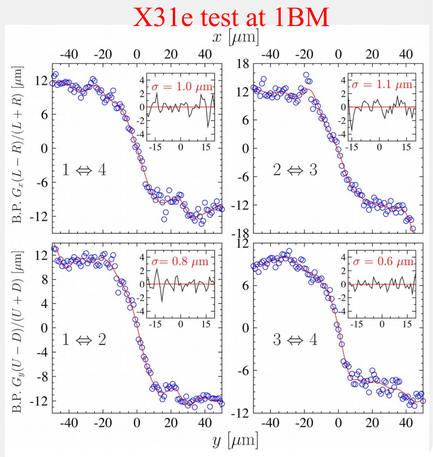

Diamond microscope (M1−M4)

They are used to monitor the x-ray beam position on the diamond crystals.

- Due to impurities in the diamond, there is significant scintillation from the diamond when it's illuminated with x-ray beams.
- Using the same camera (Prosilica) and optics (Infinity VideoMax), the diamond microscope (M1 to M4) has resolution < 10 μm.

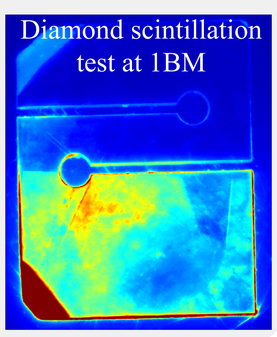

Conclusion

- All diagnostics components for the CBXFEL cavity are specified, designed, and fully characterized.
- Four types of XBPMs with resolution < 10 μm have been designed and characterized: 1) coarse alignment luminescent XBPMs; 2) microscopes for diamond crystal mirror alignment; 3) fine alignment luminescent diamond X24; and 4) fine alignment electronic quadrant diamond X31e (40 nm position sensitivity).
- Two types of XBIMs have been designed and fully characterized: 1) ns-resolution Si x-ray BIMs (sensitive to $10 - 10^7$ ph/pulse) and 2) intra-cavity diamond-based X23e (sensitive to $10^3 - 10^7$ ph/pulse).

Acknowledgment

We are grateful to Michael Wojcik, Alan Kastengren, Troy Lutes, Jeff Hoffman, Mark Engbretson, Keshab Kauchha, and Daniel Haskel for support with experiments at APS beamlines 1BM, 4ID, and 7ID. Kwang-Je Kim, Marion White, Ryan Lindberg (ANL), Zhirong Huang, Gabriel Marcus, and Alex Halavanau (SLAC) are acknowledged for helpful discussions. Work at ANL is supported by the U.S. Department of Energy, Office of Science, Office of Basic Energy Sciences, under contract No. DE-AC02-06CH11357.

Moving on from VME without Breaking the Bank

M. L. Rivers[1]

[1]Center for Advanced Radiation Sources (CARS), The University of Chicago, Chicago, IL 60637

Most APS beamlines are using VME crates as a major part of their control system. These crates mainly provide the following functions:

- Motion control: Mainly OMS-58 and MAXv controllers
- Counters, timers, MCS: Mainly Joerger scalers and SIS-3820 multi-channel scalers
- Analog output: Systran DAC128V and others
- Analog input: Acromag IP-330 and others
- Digital I/O: SBS IP-Unidig and others
- Serial communication: SBS IP-Octal and others

The VME hardware is expensive and becoming obsolete, with replacements for many of the above items no longer available. The VxWorks software is also expensive.

I am leading an effort at sector 13 to completely eliminate the 7 VME systems during the dark year. Once this is proven at sector 13, XSD and other CAT beamlines can have confidence in doing this themselves as time and resources permit.

I plan to install the following to replace the VME systems:

- Galil DMC-4183 motor controllers to replace the OMS-58 and MAXv. These will mainly be used with existing Step-Pak or Phytron driver, which reduces the cost to less than $250 per axis. This is more than 8 times less than the new ACS motion controllers that have been used on new APS beamlines.
- Moxa terminal servers to replace the VME serial communication modules.
- Measurement Computing USB-CTR08 to replace the Joerger and SIS 3820 scalers and multi-channel scaler functions. This has 8 counter channels, 4 programmable frequency generators, and 8 digital I/O. I have written EPICS support for both the scaler record and MCS support like the SIS units. Cost is about $500.
- Measurement Computing USB-3104 to replace the DAC128V for analog output. These have 8 16-bit channels which be operated in voltage output or current output mode, and 8 digital I/O. Cost is about $500.
- Measurement Computing USB-1808X to replace the IP-330. This has 8 18-bit analog inputs, 2 quadrature encoder inputs, 2 programmable frequency generators, and 4 digital I/O. It can stream analog input data at up to 200,000 samples/s. Cost is about $1,000.

The total hardware cost to replace 7 VME systems for 2 FOEs and 5 experimentation stations is less that $150K. This includes more than 370 motor channels.

Moving on from VME without Breaking the Bank

Motivation

- VME advantages: Reliable, “real-time”, lots of $$$ invested.
- VME disadvantages:
  - Poor price/performance
  - Difficult development environment
  - Aging technology: existing devices obsolete, few new devices available, local vxWorks expertise disappearing
- Need to look to alternatives for the next decades of the APS.
- Must not be too expensive since we have a “working” system.
- GSECARS plans to replace all 7 VME crates during dark year.

Measurement Computing USB-1808X ($989)

- 8 analog inputs, ±10V, ±5V, 0-10V, 0-5V ranges
  - Single-ended or differential
  - 18-bit, simultaneous sampling
- 2 analog outputs, 16-bit, +- 10V range
- 2 differential encoder inputs, 50 MHz
- 2 timing generator outputs, 50 MHz
  - Programmable frequency, duty cycle, polarity, number of pulses
- 2 counter inputs, 50 MHz
- 4 digital I/O, individually programmable direction
- Streaming input up to 200 kHz
  - Any combination of analog, encoder, counter, digital inputs
  - Up to 200 kHz
- Streaming output up to 500 kHz
  - Any combination of analog and digital outputs

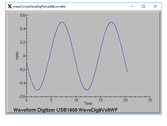

Front panel of GSECARS-designed box to house USB-1808X, USB-CTR08, and USB-3104

Current Common Beamline VME Functionality

- Analog to digital (IP-330 and others)
- Digital to analog (DAC-128V and others)
- Digital I/O (IP-Unidig and others)
- Counter/timer/MCS (Joerger VSC-16, SIS-3800, SIS-3802)
- Serial communications (IP-Octal and others)
- Allen-Bradley SLC-500 PLC communications (6008SV).

Measurement Computing USB-CTR08 ($489)

- 8 counter inputs, 48 MHz
  - 64-bit counter depth
- 4 timing generator outputs, 48 MHz
  - Programmable frequency, duty cycle, polarity, number of pulses
- 8 digital I/O, individually programmable direction
- Support for EPICS scaler record
- Support for Multi-Channel Scaler (similar to SIS 3820)
  - Minimum dwell time 250 ns per active counter
  - Can also capture value of 8 digital input bits in each dwell period

Galil DMC-4183 (~$2,000)

- 8-axis motion control
- About 8 times less expensive than ACS or Newport XPS controllers
- Pulse and direction output
  - Compatible with Step-Pak and Phytron drivers
  - Replaces VME OMS-58 and MAXv
- Optional on-board stepper and servo drivers
  - $400 for 8 axis of stepper motor drivers up to 1.4 A/phase
  - Programmable drive current and holding current
- Complex multi-axis coordinated motion
- 15 MHz encoder input frequency
- Position Compare Output for triggering detectors at specific positions
- Mature EPICS driver written at Australian Synchrotron

VME Replacements at GSECARS

- Serial: 16-port Moxa terminal server
- Analog to digital: Measurement Computing USB-1808X
- Digital to analog: Measurement Computing USB-3104
- Counter/timer/MCS: Measurement Computing USB-CTR08
- Single 3-U rack mount enclosure for above, 68 BNC connectors
- Digital I/O: Above modules provide 20 DIO, E-DIO24 for >20
- Motion control: Galil DMC-4183 8-axis controller

Measurement Computing USB-3104 ($519)

- 8 16-bit analog outputs, ±10V, 0-10V ranges
  - Synchronous update input
- 8 digital I/O, individually programmable direction
- 1 counter input 1 MHz maximum frequency

Galil Packaging at GSECARS

1) 16-channel (2 DMC-4183, RJ-45 to Step-Pak, BNC step-out
2&3) 8-channel with 1.4A stepper drivers, ELCO connectors
4) 8-channel with 3.0 A stepper drivers, ELCO connectors

Wide-field Histotomography: Sub-micron Pixel Size at Centimeter Scale for Micro-CT

Maksim A. Yakovlev[1,2,3], Carolyn R. Zaino[1,2], Daniel J. Vanselow[1,2], Steve Y. Wang[4], Patrick J. La Riviere[5], Steven L. Senft[6], Roger T. Hanlon[6], and Keith C. Cheng[1,2]

[1]Department of Pathology, Penn State College of Medicine, Hershey, PA 17033
[2]The Jake Gittlen Laboratories for Cancer Research, Penn State College of Medicine, Hershey, PA 17033
[3]Biomedical Sciences PhD Program, Penn State College of Medicine, Hershey, PA 17033
[4]Mobile Imaging Innovations, Inc., Palatine, IL 60067
[5]Department of Radiology, The University of Chicago, Chicago, IL 60637
[6]Marine Biological Laboratory, Woods Hole, MA 02543

Ideal three-dimensional imaging of complex samples consisting of micron-scale structures extending over mm to cm, such as biological tissues, requires both wide field of view and high resolution. However, most current optic systems and detectors used for micro-CT (computed tomography) imaging can only achieve sub-micron pixel resolution over fields of view of <2 mm. To improve the capability of micro-CT imaging that encompasses large, cm-scale specimens while retaining the ability to see micron-scale features, we present a unique detector system with a 1 cm field-of-view image circle and 0.7 μm pixel size that can be used in micro-CT units utilizing both synchrotron and commercial x-ray sources. Resolution and field-of-view was confirmed using a resolution-test pattern with characterized microstructures, and a whole hatchling octopus was imaged as an application of this technology at 2BM of the Argonne National Laboratory Advanced Photon Source. Volumes of 14192 × 14192 × 10640 isotropic 0.7 μm voxels were generated over a 10.0 mm × 7 mm field of view, allowing the 3-dimensional reconstruction of nerve networks that control chemotactile sensing and interarm coordination within the cm-scale sample. This unprecedented combination of field of view and resolution dramatically reduces the need for sectional scans and computational stitching for large samples, ultimately offering a way to detect changes in micron-scale morphology in the context of larger, intact model organisms and specimens. Preliminary web-based data dissemination of multiple TB-scale datasets is accomplished using Neuroglancer, allowing users to confirm scan quality through dynamically adjustable orthogonal views. This system is anticipated to benefit the global micro-CT imaging community across disciplines including materials science, microelectronics, agricultural science and biomedical engineering.

The authors are very grateful to Dr. Alan Kastengren at 7BM and to Alex Deriy, Dr. Viktor Nikin, Pavel Shevchenko, and Dr. Francesco de Carlo at 2BM of the Argonne National Laboratory Advanced Photon Source for their crucial assistance in temporarily integrating our detector with their hutch, data acquisition, and other intellectual contributions to the performed work.

Wide-Field Histotomography: Sub-Micron Pixel Size at Centimeter Scale for Micro-CT

Maksim A. Yakovlev[1,2,3], Carolyn R. Zaino[1,2], Daniel J. Vanselow[1,2], Steve Y. Wang[4], Patrick J. La Riviere[5], Steven L. Senft[6], Roger T. Hanlon[6], and Keith C. Cheng[1,2]

(1) Department of Pathology, Penn State College of Medicine, Hershey, Pennsylvania, USA; (2) The Jake Gittlen Laboratories for Cancer Research, Penn State College of Medicine, Hershey, Pennsylvania, USA; (3) Biomedical Sciences PhD Program, Penn State College of Medicine, Hershey, Pennsylvania, USA; (4) Mobile Imaging Innovations, Inc., Palatine, Illinois, USA; (5) Department of Radiology, The University of Chicago, Chicago, USA; (6) Marine Biological Laboratory, Woods Hole, 02543, MA, USA

Ideal three-dimensional imaging of complex samples consisting of micron-scale structures extending over mm to cm, such as biological tissues, requires both **wide field of view and high resolution**. However, most current optic systems and detectors used for micro-CT (computed tomography) imaging can only achieve sub-micron pixel resolution over fields of view of <2 mm. To improve the capability of micro-CT imaging that encompasses large, cm-scale specimens while retaining the ability to see micron-scale features**,** we present a unique detector system with a **1 cm field-of-view image circle and 0.7 µm pixel size** that can be used in micro-CT units utilizing both synchrotron and commercial X-ray sources. Resolution and field-of-view was confirmed using a resolution-test pattern with characterized microstructures, and a whole hatchling octopus was imaged as an application of this technology at 2BM of the Argonne National Laboratory Advanced Photon Source. Volumes of 14192 × 14192 × 10640 isotropic 0.7 µm voxels were generated over a 10.0 mm × 7 mm field of view, allowing the 3-dimensional reconstruction of nerve networks that control chemotactile sensing and interarm coordination within the cm-scale sample. This unprecedented combination of field of view and resolution dramatically reduces the need for sectional scans and computational stitching for large samples, ultimately offering a way to detect changes in micron-scale morphology in the context of larger, intact model organisms and specimens. Preliminary web-based data dissemination of multiple TB-scale datasets is accomplished using Neuroglancer, allowing users to confirm scan quality through dynamically adjustable orthogonal views. This system is anticipated to benefit the global micro-CT imaging community across disciplines including materials science, microelectronics, agricultural science and biomedical engineering.

Disciplines utilizing micro-CT imaging necessitate the generation of large-field, high resolution 3D data

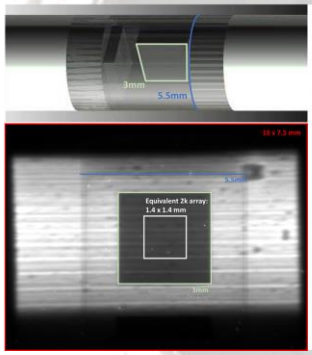

The rapid development of CMOS sensors for both consumer and commercial imaging led to the availability of cameras with over 100 million pixels and excellent noise performance at reasonable cost levels.

We developed a custom objective lens matching an Advanced Photo System-size 151MP CMOS sensor. Our custom detector represents a factor of 38× gain in field-of-view (FOV) area compared to a standard 2k pixel detector, enabling more extensive studies of complex samples in the mm to cm scale.

(A) Using a QRM-produced phantom for micro-CT we demonstrate (B) the field-of-view of our detector, encompassing the entire beam height of 2BM at 25 kV. An FOV of a standard 2k pixel array with the same resolution is shown in white.

Micron resolution was qualitatively confirmed using characterized phantom features

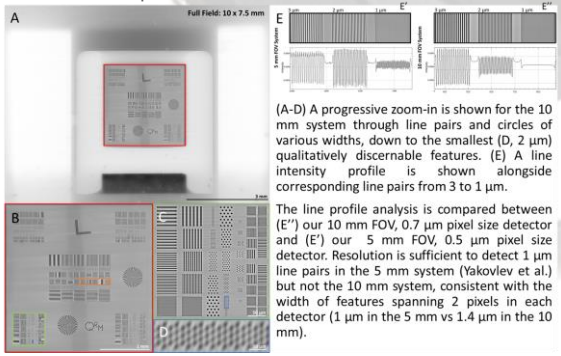

(A-D) A progressive zoom-in is shown for the 10 mm system through line pairs and circles of various widths, down to the smallest (D, 2 µm) qualitatively discernable features. (E) A line intensity profile is shown alongside corresponding line pairs from 3 to 1 µm.

The line profile analysis is compared between (E'') our 10 mm FOV, 0.7 µm pixel size detector and (E') our 5 mm FOV, 0.5 µm pixel size detector. Resolution is sufficient to detect 1 µm line pairs in the 5 mm system (Yakovlev et al.) but not the 10 mm system, consistent with the width of features spanning 2 pixels in each detector (1 µm in the 5 mm vs 1.4 µm in the 10 mm).

Micron resolution was quantitatively measured as a modulation transfer function derived from a line response

(A) A 100-projection series was taken on the 10 mm detector at the same angle of the indicated area of the slanted L edge and (B) was used to record the associated averaged intensity line profile. (C) The LSF was taken as the first derivative of pixel distance, and (D) the MTF was calculated as the discrete normalized Fourier transform of the portion of (C) covering the edge. (C) The full width at half-maximum amplitude of the LSF was recorded at 1.53 µm, with (D) the indicated 0.1 MTF amplitude located at 0.55 line pairs per µm. Edge enhancement can be visualized in the intensity profile, and calculated resolution is consistent with the qualitatively obtained results, allowing visualization of 2 µm but not 1 µm line pairs.

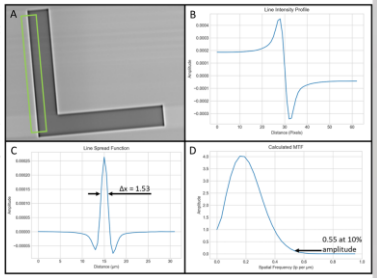

Anatomic features of interest of a 3-day old octopus are discernable across multiple tissue types in the whole cm-scale sample

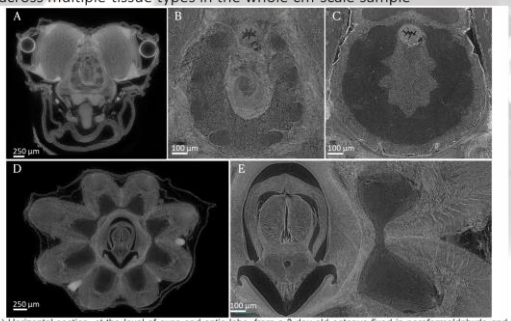

(A) Horizontal section, at the level of eyes and optic lobe, from a 3-day old octopus fixed in paraformaldehyde and stained with phosphotungstic acid and eosinY. Brachial nerves, to and from each of the 8 arms, are visible in the middle of the image, just below the esophagus. (B) Detail of brachial nerves at a more central (CNS) level, entering the prebrachial lobe; esophagus at top with unpaired aorta to right below it. (C) Brachial nerve terminations continuing on towards postbrachial lobe neuropil (note cell body clusters centrally and circumferentially). (D) Peripheral portions of the brachial nerves, as they enter each arm, surrounding the buccal mass. Note several inter-arm connectives. (E) Detail of two arms and a connective. Note that many individual muscle fibers are resolvable. Buccal apparatus at left.

Preliminary dissemination of 7TB scan volumes is accomplished through Neuroglancer and Syglass

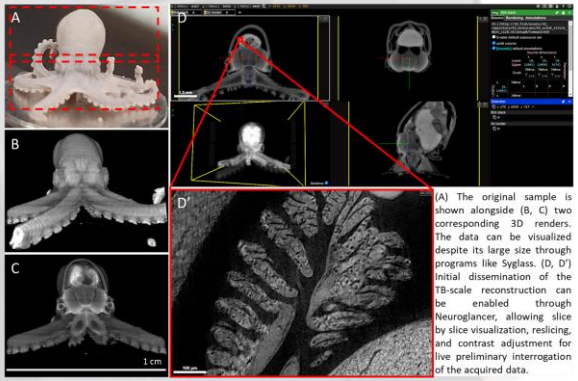

(A) The original sample is shown alongside (B, C) two corresponding 3D renders. The data can be visualized despite its large size through programs like Syglass. (D, D') Initial dissemination of the TB-scale reconstruction can be enabled through Neuroglancer, allowing slice by slice visualization, reslicing, and contrast adjustment for live preliminary interrogation of the acquired data.

Acknowledgements

This research was funded by the National Institutes of Health (PI: KCC, R24-RR017441, and PI: KCC, R24-0D018559), The Jake Gittlen Laboratories for Cancer Research, the Huck Institutes of the Life Sciences and the Institute for Cyber Science, and the Office of Naval Research (PI: RTH, N00014-22-1-2208). This research used resources of the Advanced Photon Source, a U.S. DOE Office of Science User Facility. The authors are very grateful to **Dr. Alan Kastengren** at 7BM and to **Alex Deriy, Dr. Viktor Nikitin, Pavel Shevchenko, and Dr. Francesco de Carlo** at 2BM of the Argonne National Laboratory Advanced Photon Source for their crucial assistance in temporarily integrating our detector with their hutch, data acquisition, and other intellectual contributions to the performed work.

References

Yakovlev, M. A., Vanselow, D. J., Ngu, M. S., Zaino, C. R., Katz, S. R., Ding, Y., Parkinson, D., Wang, S. Y., Ang, K. C., La Riviere, P. J. et al. A wide-field micro-computed tomography detector: micron resolution at half-centimetre scale. J. Synchrotron Radiation. 2021; 29, 505-514. https://doi.org/10.1107/S160057752101287X

Babaei F, Hong TL, Yeung K, Cheng SH, Lam YW. Contrast-Enhanced X-Ray Micro-Computed Tomography as a Versatile Method for Anatomical Studies of Adult Zebrafish. Zebrafish. 2016; 13(4):310-6. doi: 10.1089/zeb.2016.1245. Epub 2016 Apr 8. PMID: 27058023.

Umetani K, Okamoto T, Saito K, Kawata Y, Niki N. 36M-pixel synchrotron radiation micro-CT for whole secondary pulmonary lobule visualization from a large human lung specimen. Eur J Radiol Open. 2020; 7:100262. doi: 10.1016/j.ejro.2020.100262. PMID: 32984451; PMCID: PMC7495051.

ZAO® Based Non-evaporable Getter Pumps in Optics Vacuum Chambers

Steven Wulfsberg[1], Carlo Santini[1], Enrico Maccallini[1], Andrea Cadoppi[1], Dario Nicolosi[1], Marco Urbano[1], Paolo Manini[1], Michele Mura[1], and Fabrizio Siviero[1]

[1]SAES Group, S.p.A, 20020 Lainate (MI), Italy

The pumping systems in optical vacuum chambers play a critical role and with enough speed, they can also help reduce issues such as carbon contamination of the optics' surface. Multiple accelerator facilities have qualified SAES' ZAO NEG pump in particle sensitive applications, such as optics chambers, due to the minimization of particle generation by the ZAO NEG material.

The ZAO NEG pumps provide 1000s of liters per second of pumping for CO and CO_2 in a very compact size (4 x 8 inches) and light weight (maximum 9 lbs.) design. The high pumping performance for these gases is important because CO and CO_2 have been shown to be precursor molecules for carbon contamination via X-ray photon induced dissociation. The ZAO NEG pumps provide 100s of liters per second of pumping for hydrocarbons as well, removing them from the vacuum before they are cracked and deposited onto the mirrors and monochromators. In any application, the combination of ZAO NEG element with a compact ion pump in the NEXTorr® concept can further optimize the distribution of pumping for all gases, including hydrocarbons. Additionally, the ZAO NEG pumps present the following benefits:

- Significantly higher degrees of activation at lower temperatures relative to other NEG pumps, with insignificant power irradiation during a two hour activation.
- NEG pumps do not need power during standard operation after the activation procedure.
- With the HV series, ZAO NEG pumps can operate in the high vacuum pressure range and can start their activation at 1e-2 Torr, providing fast pumpdown during quick maintenance work.

The ZAO NEG pumps are available as standalone NEG pumps, integrated compact ion and NEG pumps in the NEXTorr concept, and flangeless wafer modules. These ZAO based NEG pumps provide benefits from the first pumpdown to the UHV level without interfering with mirror and monochromators systems in terms of particle generation, thermal irradiation, and generation of magnetic field.

ZAO® Based Non Evaporable Getter Pumps in Optics Vacuum Chambers

Steven Wulfsberg, Carlo Santini, Enrico Maccallini, Andrea Cadoppi, Dario Nicolosi, Marco Urbano, Paolo Manini, Michele Mura, and Fabrizio Siviero
SAES Group, S.p.A, 20045 Lainate (MI), Italy

Optics chambers need high pumping speeds and suffer from carbon contamination

- Components in optics chambers outgas hydrocarbons that cause carbon contamination on the surfaces of optics.
- Studies suggest CO and CO_2 also contribute to carbon contamination via photon stimulated dissociation by the X-ray beam.
- This is visually evidenced by the black stripe of carbon contamination commonly found where the X-rays strike the optics' surface.

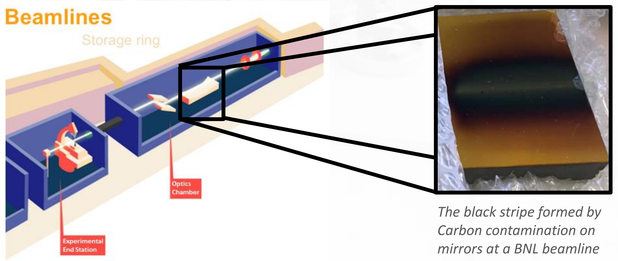

The beamlines that house the optics chambers (esrf.fr)

The black stripe formed by Carbon contamination on mirrors at a BNL beamline

Consequently, high pumping speeds for CO and CO_2 can help reduce and prevent the formation of carbon contamination.

SAES ZAO pumps with the ZAO® NEG alloy provide high pumping speeds for CO, CO_2 H_2, and hydrocarbons while maintaining compact, lightweight designs

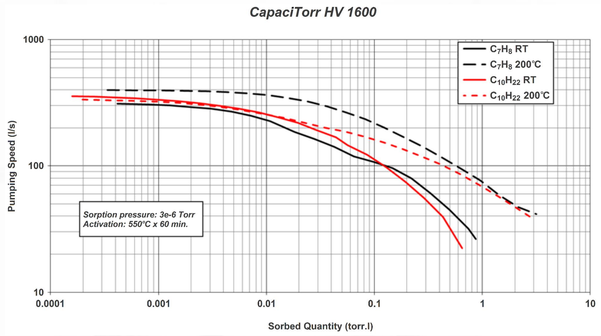

- **Hydrocarbon** pumping speeds up to **600 l/s**
- **CO** pumping speeds up to **1400 l/s**
- **H2** pumping speeds up to **3900 l/s**

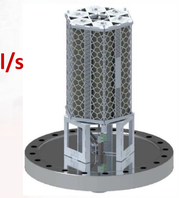

SAES NEG Pump portfolio, including the SAES ZAO pumps

ZAO CapaciTorr Z Series NEG Pumps				
Pump	Pumping Speed, l/s		Flange size	Weight, kg (lbs.)
	H_2	CO		
CapaciTorr Z 100	150	65	CF35/2.75"	0.4 (0.9)
CapaciTorr Z 200	290	130	CF35/2.75"	0.5 (1.1)
CapaciTorr Z 400	500	210	CF63/4.50"	0.7 (1.5)
CapaciTorr Z 1000	1250	550	CF63/4.50"	1.6 (3.5)
			CF100/6.00"	2.1 (4.6)
CapaciTorr Z 3500	3900	1400	CF150/8.00"	6.5 (14.3)
			CF200/10.0"	7.5 (16.5)

Optics chambers can be sensitive to thermal radiation, specifically with the optics

SAES ZAO pumps:

- Are capable of a higher degree of activation at lower temperatures compared to the previous generation of SAES D series (St172 NEG alloy) and generic NEG pumps.
- Decrease thermal irradiation and dispersion, which minimizes the pump's effects on the temperature and thermal properties of the optics.

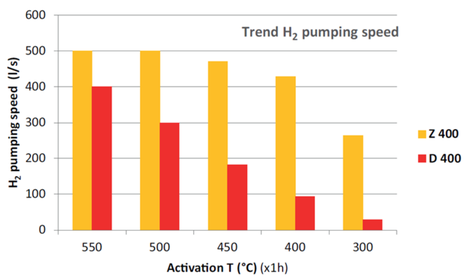

- The graph below reports the degree of activation at different temperatures for the Z 400 (ZAO NEG alloy) vs. D 400 (St172 NEG alloy).
- At 400 °C, the Z 400 is approximately 95% activated, but the D 400 is less than 25% activated. This shows the profound advancement of the ZAO NEG material.

Optics chambers are sensitive to particle generation

SAES ZAO pumps:

- Meet the low-particle requirements of optics chambers.
- Are validated and successfully employed in particle sensitive applications such as photocathode chambers, electron microscopes, beamline optics chambers, and cold trap systems.
- Meet the rigorous low particle requirements of the high-gradient SRF cavities at Jefferson Lab.

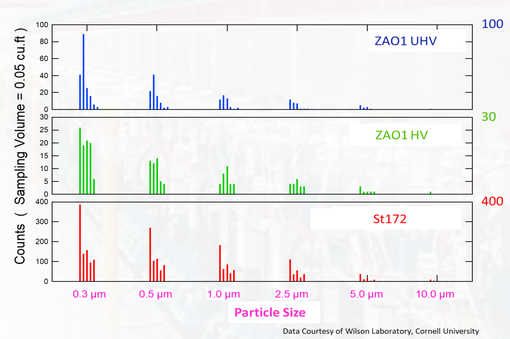

Data Courtesy of Wilson Laboratory, Cornell University

- The chart above reports that the ZAO NEG alloy produces:
  - Extremely low particles counts.
  - Significantly less particles than the St172 sintered NEG pumps.

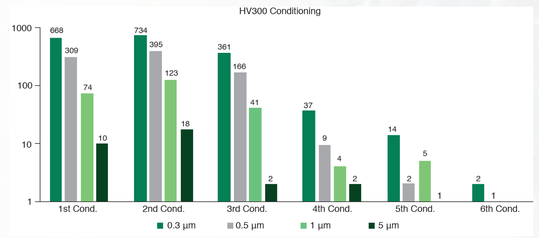

- The graph above reports particle count data for the ZAO NEG pumps for qualification in the particle sensitive European Spallation Source (ESS) accelerator.
- The SAES ZAO NEG pumps passed with flying colors!
- After a few conditioning cycles, the ZAO NEG pumps were practically particle free. A truly state of art feature for the SAES ZAO NEG pumps.

SAES ZAO pumps versus the traditional large pumping systems

- Large, bulky, and heavy pumps can create maintenance, structural, and spatial challenges.
- SAES NEXTorr ZAO NEG pumps integrate the NEG pump and the ion pump into a compact, lightweight, and elegant design that a signal person can lift and remove
- SAES ZAO NEG pumps are bringing 100s and 1000s of liters per second of pumping to optics chambers around the world.
- Synchrotron facilities in North America and Europe have already integrated SAES ZAO NEG pumps into their beamlines and optics chambers.
- And more are incorporating them into their designs for new projects and upgrades

Conclusions

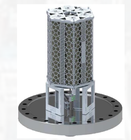

- **ZAO NEG** pumps provide **high CO, CO_2, H_2, and hydrocarbon pumping speeds.**
- **ZAO NEG** pumps are capable of a **higher degree of activation at lower temperatures.**
- **ZAO NEG** pumps meet the **low particle requirements of optics chambers.**
- **SAES ZAO NEG** pumps deliver 100s and 1000s of liters per second of pumping in **compact, lightweight, and elegant designs.**

SCIENTIFIC INSTRUMENTS
CINEL®

Surface Modification and its Impact on HgTe Colloidal Quantum Dots and Devices

Matthew Ackerman[1], Edward Malachosky[1]

[1]QDIR Inc., Chicago, IL 60615

Colloidal quantum dots (CQDs) afford the advantages of wavelength tunability, low-cost production, and scalability thanks to their nanoscale size and solution processability. However, the high surface energy of these quantized semiconductor nanocrystals makes their functional characteristics prone to environmental effects, such as chemical and temperature, that can degrade or modify their optical and electronic properties. QDIR and its team are working at the Center for Nanoscale Materials to understand and overcome these limitations for mercury telluride (HgTe) CQDs to produce high-performance and low-cost CQD-based infrared detectors beyond 1000 nm. In this work, we report on the impact of chemical and temperature effects on the optical and electronic properties of the HgTe CQD materials and share the results of methods used to modify and passivate their surfaces against these degradation processes. The results of this work motivate the need for continued investigation into methods to manipulate CQD surfaces to produce functional, commercial electronic and optoelectronic CQD-based devices.

Work performed at the Center for Nanoscale Materials, a U.S. Department of Energy Office of Science User Facility, was supported by the U.S. DOE, Office of Basic Energy Sciences, under Contract No. DE-AC02-06CH11357.

Surface Modification And Its Impact On HgTe Colloidal Quantum Dots And Devices

Matthew Ackerman[1], Edward Malachosky[1]

[1]QDIR Inc., Chicago, IL, 60615

Introduction

Colloidal quantum dots (CQDs) afford the advantages of wavelength tunability, low-cost production, and scalability thanks to their nanoscale size and solution processability. However, the high surface energy of these quantized semiconductor nanocrystals makes their functional characteristics prone to environmental effects, such as chemical and temperature, that can degrade or modify their optical and electronic properties. QDIR and its team are working at the Center for Nanoscale Materials to understand and overcome these limitations for mercury telluride (HgTe) CQDs to produce high-performance and low-cost CQD-based infrared detectors for infrared sensing beyond 1000 nm.

Motivation and Methods

The optical and electronic properties of HgTe CQDs degrade due to sintering when exposed to temperatures above 100ºC, which limits their usefulness in practical devices. Atomic layer deposition (ALD, Arradiance Gemstar XT) was investigated as a technique for introducing diffusion barriers in the film of HgTe CQDs to fill in the space between neighboring CQDs. A low-temperature ALD process was developed, optimizing the deposition conditions (dwell time, purge time, precursor concentration, number of cycles) and measuring the transmission spectra of the CQD films for spectral red-shift or broadening that are signs of sintering.

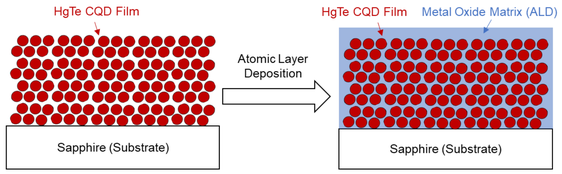

Figure 1. Cartoon of the HgTe CQD thin film coated on sapphire substrate before and after atomic layer deposition of metal oxide.

The electronic properties of CQDs vary with the choice of surface ligands, modifying the charge carrier doping and mobilities of CQD solid films. Therefore, the doping and carrier mobilities of CQD films can be tailored for engineering optoelectronic devices. Here, the surface of HgTe CQDs were modified by either solid-state ligand exchange (soaking a solid film in a dilute solution of ligand in alcohol) or solution phase exchange (transferring CQDs from non-polar to polar solvent containing select ligands) to investigate the effect on mobility and doping, extracted from the transfer curve of field effect transistor devices.

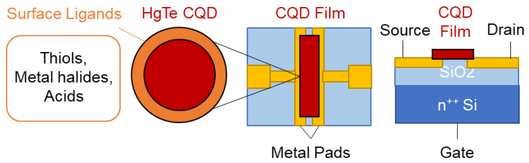

Figure 2. Schematic of the backside-gated field effect transistors used to characterize the mobility and doping of functionalized HgTe CQD films.

Results

Atomic Layer Deposition of Alumina on HgTe CQD Films – The absorption spectra of HgTe CQD films was measured before ALD, after ALD, and after subjecting the film to elevated temperatures for several hours. Broadening of the excitonic feature and red-shifting of the absorption edge are markers of CQD sintering. The degree of sintering decreases with increasing number of ALD cycles.

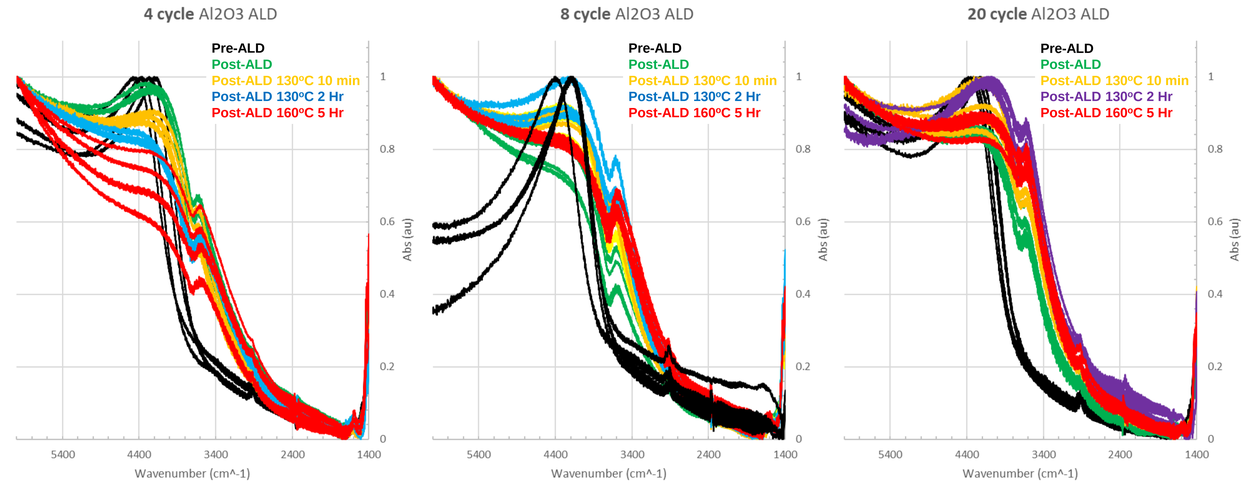

Figure 3. Absorption spectra of HgTe CQD tihin films measured as a function of process conditions for (left) four (4) cycles of alumina, (center) 8 cycles of alumina, and (right) twenty (20) cycles of alumina deposited by ALD.

Surface Ligand Modification and Effect on Doping and Mobility of HgTe CQD Films – The surface of HgTe CQDs were modified by either solid-state ligand exchange or solution phase exchange. Positive slope at positive and negative gate potential correspond to electron and hole transport, respectively. For the minimum of conductance, positive or negative gate potential correspond to p-type or n-type materials, respectively. The magnitude of the gate potential is proportional to the magnitude of the doping density.

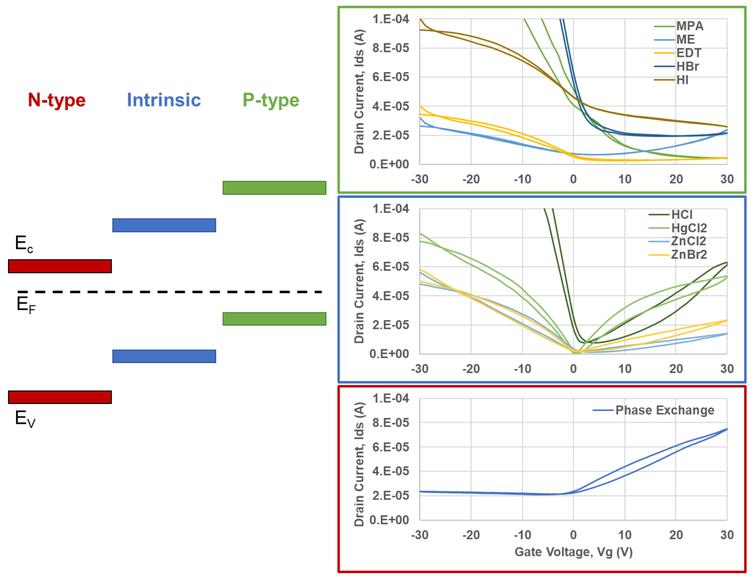

Figure 4. (Left) Simple diagram of the relative energy level positions for the conduction (E_C), Fermi (E_F), and valence (E_V) levels of the HgTe CQDs when doped n-type (excess electrons), intrinsic, and p-type (excess holes). (Right) Transfer curves measured by Field Effect Transistor separated by (Top) p-type, (Center) near-intrinsic, and (Bottom) n-type character.

Table 1. Charge carrier mobilities in HgTe CQD films calculated from FET measurements

Ligands		Mobility (cm^2/Vs)
Solid-state exchange		
Thiols	EDT	0.03
	MPA	0.15
	ME	0.02
Acids	HCl	0.37
	HBr	0.35
	HI	0.06
Metal Halides	$HgCl_2$	0.09
	$ZnCl_2$	0.05
	$ZnBr_2$	0.04
Phase Exchange		
	$HgCl_2$, ME	0.06

Abbreviations: 1,2-ethanedithiol (EDT), 3-mercaptoproptionic acid (MPA), 2-mercaptoethanol (ME)

Discussion and Conclusion

The surface modification of HgTe colloidal quantum dots plays a significant role in engineering their physical and electronic properties. Atomic layer deposition. While HgTe CQDs sinter readily near 100ºC in several minutes without any protection, as few as several cycles of alumina ALD were used as a barrier to mitigate CQD sintering up to 160ºC, presenting a great opportunity to engineered HgTe CQD films and devices with the thermal integrity required for field use in both defense and commercial applications. Additional work is required to understand the impact of ALD on the electronic properties of HgTe CQDs.

From the investigation of surface ligands, acids were the most effective ligands for improving the charge carrier mobility while the doping was more dependent on the ligands—trending p-type with thiols and nearly intrinsic with metal halides. N-type doping was not achievable with solid-state ligand exchange, so a liquid phase exchange containing excess metal halide salt was used to engineer a metal-rich HgTe CQD film with n-type character.

Finally, with doping tunable from n-type to p-type, a HgTe CQD focal plane array was demonstrated as a proof-of-concept imaging device.

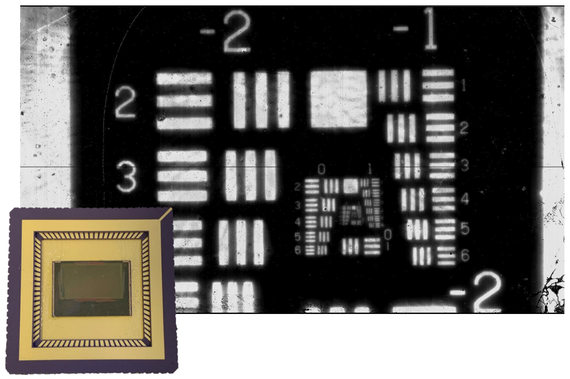

Figure 5. Shortwave infrared image of a 1951 Air Force Resolution Test Target illuminated from backside. Image captured with 1 ms integration time and f/4 CaF_2 llens on a 1280×720 format readout circuit. (Inset) Finished HgTe CQD focal plane array image sensor used to capture the image.

Acknowledgements

The authors would like to acknowledge Dr. Liliana Stan, Dr. Benjamin Diroll, and Dr. Ralu Divan for their advice and research support during this project.

Work performed at the Center for Nanoscale Materials, a U.S. Department of Energy Office of Science User Facility, was supported by the U.S. DOE, Office of Basic Energy Sciences, under Contract No. DE-AC02-06CH11357. This material is based upon work supported by the National Science Foundation under Grant No. 2112359.

QDIR

Auger Recombination in Colloidal Semiconductor Nanoplatelets

Alexandra Brumberg[1], John P. Philbin[2], Benjamin T. Diroll[3], Eran Rabani[4], and Richard D. Schaller[3]

[1]University of California, Santa Barbara, CA 93106
[2]University of California, Los Angeles, CA 90095
[3]Nanoscience and Technology Division, Argonne National Laboratory, Lemont, IL 60439
[4]University of California, Berkeley, CA 94720

Auger recombination (AR), a nonradiative recombination process in which an electron and a hole recombine and transfer its excess energy to a third carrier, negatively impacts the efficiencies of devices made from colloidal semiconductor nanocrystals (NCs) because of fast AR rates. Colloidal, two-dimensional semiconductor nanoplatelets (NPLs) offer a solution to the problem of fast AR rates in colloidal NCs while preserving other benefits of NCs such as band gap tunability and high photoluminescence efficiency. In NPLs, AR rates are reduced owing to quantum confinement in only one dimension with bulk-like lateral dimensions. However, the mix of quantum-confined and bulk-like dimensions in NPLs along the thickness and lateral axes, respectively, makes it difficult to predict their photophysical behaviors. Here, we investigate two aspects of AR in two-dimensional NPLs: (1) the scaling of AR rates with NPL area and volume, and (2) the temperature dependence of AR rates.

1: Both zero- and one-dimensional NCs have been shown to follow a “universal volume scaling” relationship for AR rates as a function of volume. However, both experimental and theoretical efforts have yet to agree on the relationship between AR rate and NPL area and volume. We combine experiment with a new theoretical model to ultimately convey that AR rates scale with NPL area but not volume.

2: Conceptually, AR is expected to transition from temperature-dependent behavior in bulk semiconductors to temperature-independent behavior in QDs as a result of flattened band structure in the latter that facilitates satisfaction of linear momentum conservation. In NPLs, the expected behavior is unknown, and AR as a function of temperature has never been studied. We investigate the temperature dependence of biexciton lifetime and fluence-dependent emission in colloidal CdSe NPLs and compare the behavior to that observed with QDs. For NPLs, upon temperature reduction, biexciton lifetime surprisingly decreases and emission intensity increases nearly linearly with fluence rather than saturating, consistent with dominant radiative recombination rather than nonradiative AR. Notably, this suggests that NPLs differ fundamentally from isotropic NCs, and that AR cannot be assumed to be the dominant recombination mechanism for all NCs across all temperatures.

Auger Recombination in Colloidal Semiconductor Nanoplatelets

Alexandra Brumberg[1], John P. Philbin[2], Benjamin T. Diroll[3], Eran Rabani[2], Richard D. Schaller[1,3]

1 Auger recombination

Auger recombination (AR) is a **nonradiative recombination** process in which an electron and a hole recombine and nonradiatively transfer their excess energy to a third carrier (either an electron or a hole).

scheme of AR in NCs

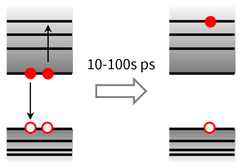

In semiconductor nanocrystals (NCs), AR:

- is very fast (10-100s ps)
- affects performance of devices (e.g. LEDs)

efficiency reduction at high powers in LEDs

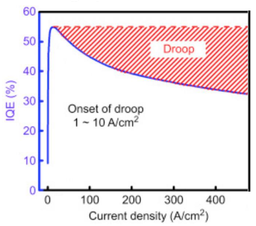

Understanding the mechanism and fundamentals of AR is crucial to improving the performance of many types of nanotechnology.

Fu and Zhao. *Nitride Semiconductor LEDs*, 2nd ed; Woodhead Publishing Series, 2018.

2 Colloidal nanoplatelets

Nanoplatelets (NPLs) are **colloidal, two-dimensional semiconductor NCs**.

- Thickness (atomically precise) determines the band gap
- Lateral area does not affect the band gap significantly

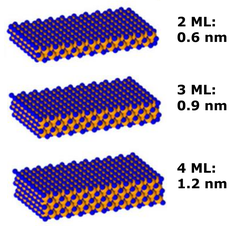

Advantages of NPLs:

- Large absorption cross-sections
- Narrow emission
- Polarized emission
- Directional electronic transport
- **Reduced rates of AR!**

Predicting and understanding AR in NPLs is difficult because of their 2D nature, which combines both quantum and bulk-like properties.

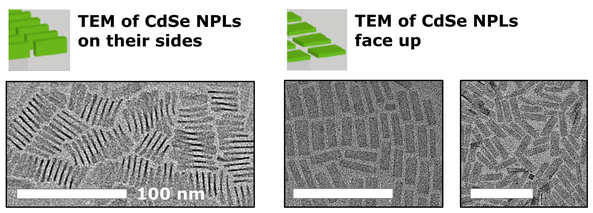

Ott et al. *Nano Lett.* **2017**, *17*, 6870

3 Universal scaling law

In 0D and 1D NCs:

- AR scales linearly with NC volume ("**universal scaling law**")

In 2D NPLs:

- She *et al.* reported constant AR lifetimes, independent of NPL area
- Li and Lian reported AR lifetimes that scale linearly with NPL area

What is the dependence of AR lifetime on NPL area and volume?

universal scaling of AR in 0D quantum dots

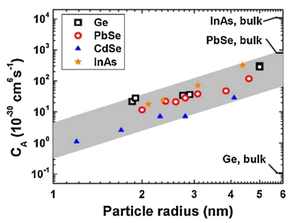

unknown scaling in 2D NPLs

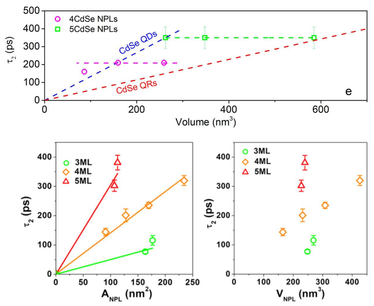

Robel *et al. Phys. Rev. Lett.* **2009**, 102, 177404
She *et al. ACS Nano*, **2015**, *9*, 9475
Li and Lian. *Nano Lett.* **2017**, *17*, 3152

4 Interacting formalism

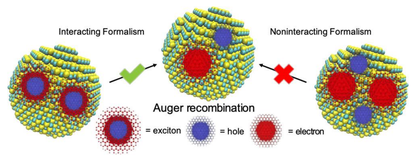

Noninteracting formalism:

- Ignores all the electron-hole interactions in the biexciton (i.e. four separate carriers)
- Traditional way of modeling AR but is not effective for NCs

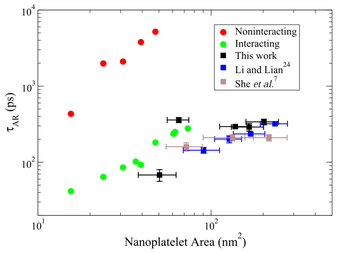

Interacting formalism:

- Includes spatial correlations within the electron-hole pairs, but ignores the correlation between the excitons
- Consistent with a large exciton binding energy but low biexciton binding energy

Both experiment and theory support AR lifetimes that scale linearly with area. Some remaining open questions:

- Do AR lifetimes saturate at large NPL areas?
- What is the scaling with NPL thickness? (theory does show a power law dependence)

Philbin and Rabani. *Nano Lett.* **2018**, *18*, 7889
Philbin, Brumberg, *et al. J. Chem. Phys.* **2020**, *153*, 054104

5 Temperature dependence

Bulk semiconductors
Temperature-dependent AR due to conservation of momentum

Quantum dots
Temperature-independent AR due to relaxed conservation of momentum

Nanoplatelets
Temperature behavior unknown

What is the effect of temperature (i.e. momentum) on AR rates in NPLs, given quantum confinement in only one dimension?

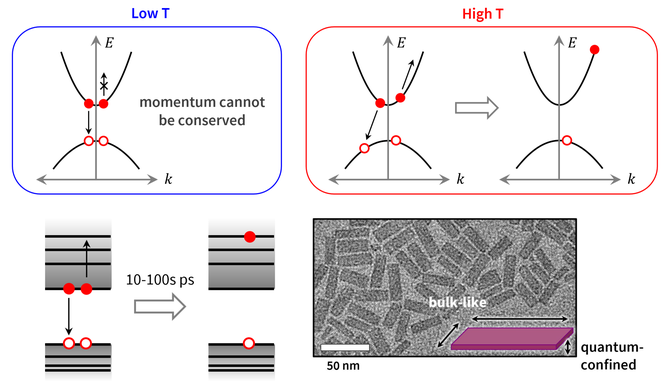

6 Radiative biexcitons

Measurements of the biexciton lifetime (making no assumptions about radiative vs nonradiative recombination) show a **decrease** in biexciton lifetime as the temperature drops!

- Bulk-like Auger would show increase in AR lifetime
- Quantum-like Auger would exhibit no temperature dependence

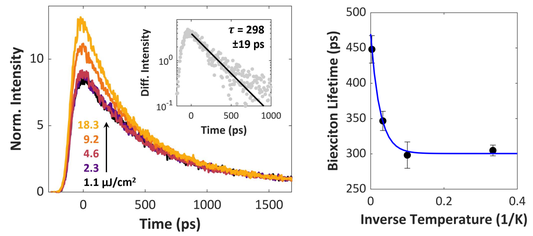

This suggests a significant **radiative** component in biexciton recombination – highly unusual for semiconductor NCs!

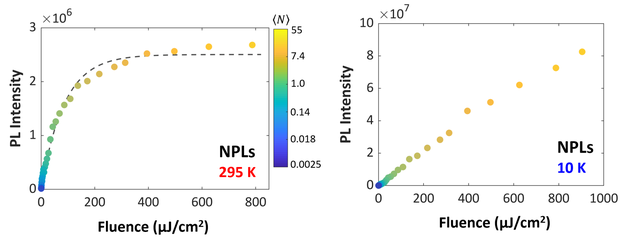

Measurements of integrated photoluminescence intensity indicate:

- At room temperature, multiexcitons recombine primarily through nonradiative recombination pathways (like quantum dots)
- At 10 K, multiexcitons recombine primarily through radiative recombination

Brumberg *et al. Nano Lett.* **2022**, *22*, 6997

7 Acknowledgements

Author affiliations:
1 – Department of Chemistry, Northwestern University, Evanston, IL, USA
2 – Department of Chemistry, University of California, Berkeley, CA, USA
3 – Center for Nanoscale Materials, Argonne National Laboratory, Lemont, IL, USA

Progress in Fabrication of Free-standing Gold Membrane-mask for Phase-based Soft X-ray Microscopy

O.V. Makarova[1], R. Divan[2], N. Moldovan[2,3], D.A Czaplewski[2], M. Esposito[4], C.-M.Tang[5], J.D. Ferrara[6], and A. Olivo[4]

[1]Creatv MicroTech, Inc., Chicago, IL 60612
[2]Center for Nanoscale Materials, Argonne National Laboratory, Lemont, IL 60439
[3]Alcorix Co., Plainfield, IL 60544
[4]Department of Medical Physics and Biomedical Engineering, University College London, London WC1E 6BT, United Kingdom
[5]Creatv MicroTech, Inc., Rockville, MD 20850
[6]Rigaku Americas Corp, The Woodlands, TX 77371

We are developing a phase-based soft x-ray microscope allowing to obtain high-resolution high-contrast 3D images of biological samples using an incoherent, rotating anode x-ray source. The use of 8 keV x-rays for maximum soft-tissue sensitivity, required a freestanding mask, as any substrate (such as those used by gratings) would absorb a significant fraction of the available flux.

The first mask prototype - a 10-μm-thick gold membrane with an array of micrometer-wide and 400-micrometer-long void slit apertures with 7.5-μm periodicity has been fabricated and an aperture-driven spatial resolution has been demonstrated.

Here, we present the progress towards a refined process allowing to obtain submicron aperture slits (700 nm) and to substantially improve gold membrane flatness (below 200 nm over the entire 4 mm x 4 mm area) for higher x-ray imaging resolution.

The research was supported by the National Institute of Health under Award Number R01EB028829. Work performed at the Center for Nanoscale Materials, a U.S. Department of Energy Office of Science User Facility, was supported by the U.S. DOE, Office of Basic Energy Sciences, under Contract No. DE-AC02-06CH11357. AO is supported by the Royal Academy of Engineering under the Chair in Emerging Technologies scheme (CiET1819/2/78).

Progress in fabrication of free-standing gold membrane-mask for phase-based soft X-ray microscopy

O.V. Makarova[1], R. Divan[2], N. Moldovan[2,3], D.A Czaplewski[2], M. Esposito[4], C.-M.Tang[5], J.D. Ferrara[6] and A. Olivo[4]

[1] *Creatv MicroTech, Inc., 2242 West Harrison St., Chicago IL 60612*

[2] *Center for Nanoscale Materials, Argonne National Laboratory, Argonne IL 60439*

[3] *Alcorix Co., 14047 Franklin Ct., Plainfield IL 60544*

[4] *Department of Medical Physics and Biomedical Engineering, University College London, London WC1E 6BT, United Kingdom*

[5] *Creatv MicroTech, Inc., 9900 Belward Campus Drive, Rockville, MD 20850*

[6] *Rigaku Americas Corp, The Woodlands, TX 77371*

Abstract

- We are developing a phase-based soft X-ray microscope allowing to obtain high-resolution high-contrast 3D images of biological samples using an incoherent, rotating anode X-ray source by analyzing the sample-induced changes "tracked" by the detector.
- The use of 8 keV X-rays for maximum soft-tissue sensitivity, required a freestanding mask, as any substrate such as those used by gratings) would absorb a significant fraction of the available flux.
- The first mask prototype - a 10-µm-thick gold membrane with an array of µm-wide and 400 µm-long void slit apertures with 7.5-µm periodicity has been fabricated and an aperture-driven spatial resolution has been demonstrated [1].
- We present the progress towards a refined process allowing to obtain submicron aperture slits and to substantially improve gold membrane flatness for higher X-ray imaging resolution.

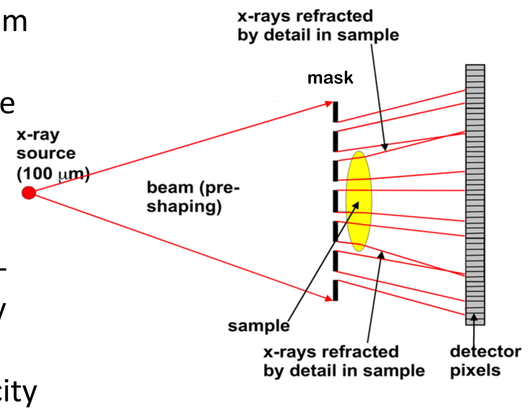

Fabrication

Wafer front

Lithography and Si DRIE — SiN_x, SiO_2, Cr/Au — SiO_2 lift-off — Gold plating — Flip over

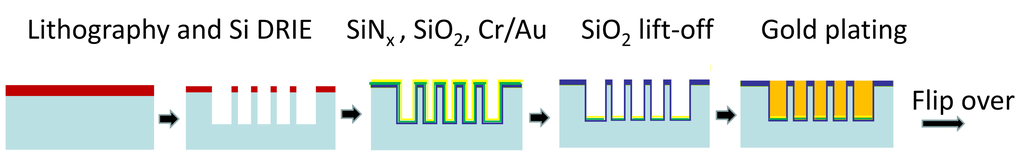

Wafer back

DRIE — Carrier removal, clean — Si, SiN_x, SiO_2 dry etch

Gold membrane mask

Si S1805 Cr/Au Au SiN_x SiO_2 AZ4620

SiN_x is used as an insulation and SiO_2 as a lift-off layers for creating a plating base at the bottom of the grooves for subsequent gold electroplating, followed by Si back-etch to obtain the gold membrane mask.

Results

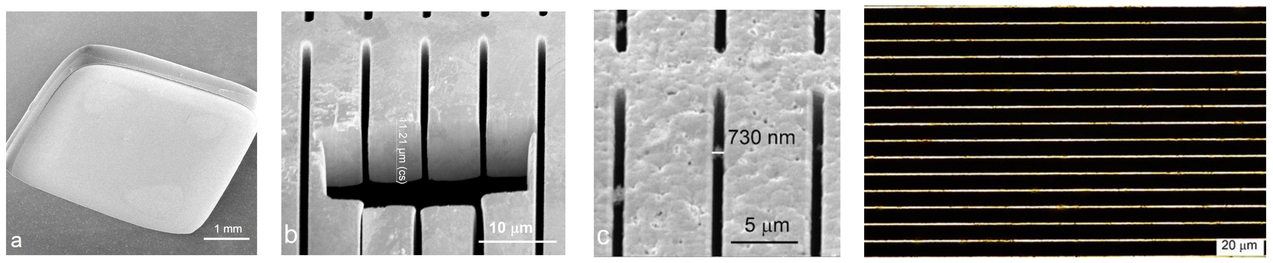

SEM images of the backside of the mask at 45° :

(a) general view of 4x4 mm² gold membrane in Si; grid lines are not visible because of limits in resolution at this magnification;

(b, c) 11-µm-thick freestanding gold membrane mask with arrays of 0.9- and 0.7-µm-wide void apertures with 7.5 µm periodicity. Image (b) was obtained after focused ion beam cross sectioning;

(d) Optical image taken with back illumination shows parallel 0.7-µm-wide void apertures of the gold membrane gratings. The aperture length of 400 µm is determined by 3-µm-wide gold buttresses.

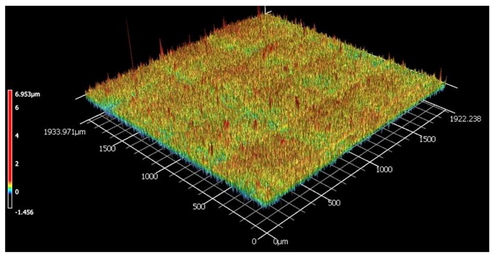

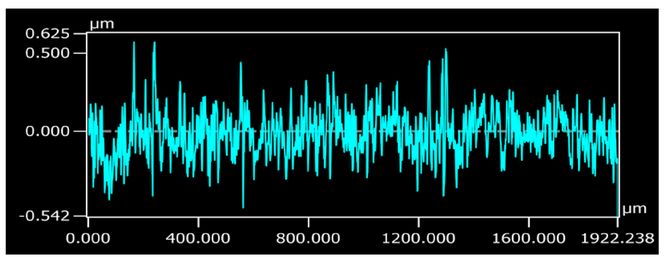

Optical flatness measurements of the freestanding gold grating performed with a laser confocal microscope. 3D profile of a portion of 1.9 mm x 1.9 mm of the grating area, with the Z-axis expanded 100 times compared to lateral coordinates, showing a flatness of the order of the gold roughness. Line scan normal to the grid lines showing flatness deviations from the ideal planar shape below 0.2 µm.

Summary

- A microfabrication process was developed to fabricate the mask prototypes for a novel low-energy, phase-based X-ray microscope.
- The method developed herein allows for further increase in the aspect ratio as we target higher resolution (i.e., narrower apertures) or higher x-ray energies, which are among our plans for future development.
- Future work will focus on further reducing aperture width down to 500 nm and on the optimization of the fabrication parameters for reliable manufacturing of the freestanding masks.

[1] O.V. Makarova, R. Divan, N. Moldovan, D.A Czaplewski, M. Esposito, M. Endrizzi, C-M Tang, J.D. Ferrara and A. Olivo, Nanotechnology 2023, 34, 045301.

The research was supported by the National Institute of Health under Award Number R01EB028829. Work performed at the Center for Nanoscale Materials, a U.S. Department of Energy Office of Science User Facility, was supported by the U.S. DOE, Office of Basic Energy Sciences, under Contract No. DE-AC02-06CH11357. AO is supported by the Royal Academy of Engineering under the Chair in Emerging Technologies scheme (CiET1819/2/78).

Geometric Confinement and Proximity Effects on Magnetic Textures in Nanoscale Patterned Magnetic Thin Films

Kayna L. Mendoza Trujillo[1,2*], Ralu Divan[2,3], Yue Li[2], Yi Jiang[2,4], Arthur R. C. McCray[2,5], Amanda K. Petford-Long[1,2], and Charudatta Phatak[1,2]

[1]Department of Materials Science and Engineering, Northwestern University, Evanston, IL 60208
[2]Materials Science Division, Argonne National Laboratory, Lemont, IL 60439
[3]Center for Nanoscale Materials, Argonne National Laboratory, Lemont, IL 60439
[4]Advanced Photon Source, Argonne National Laboratory, Lemont, IL 60439
[5]Applied Physics Program, Northwestern University, Evanston, IL 60208

Miniaturization of electronics relies on the exploitation of material properties, specifically magnetic and electronic, as a function of reduced dimensionality. As the electronics industry transitions to nano-electronic technologies, it is critical that we understand the fundamental physics and dynamic behaviour of topologically, non-trivial spin states at the atomic and nano-scale limit that can be used for information storage. As such, we utilize a maskless lithographic technique in fabricating magnetic thin films, namely electron beam lithography, directly atop transmission electron microscopy (TEM) silicon-nitride (SiN_x) membranes. Physical vapor deposition techniques such as magnetron sputtering and/or evaporation deposition are used to build the nano-scale magnetic thin films. We then directly observe the magnetic domains, film morphology, and defects in a field-free environment by using aberration-corrected Lorentz TEM (ALTEM).

This work highlights the fabrication of micro- to nano-scale islands of magnetic thin films of Cr(2 nm)/$Ni_{80}Fe_{20}$(16 nm)/Cr(2 nm), and capped with a carbon (< 1 nm) de-charging layer in a USAF resolution test pattern structure using the above mentioned processes. We were successfully able to pattern islands with inter-island spacing as small as 35 nm ± 15 nm with dimensions of 283.1 nm by 52.4 nm. Additionally, we will present two open-access models based on the transport-of-intensity equation[1] and reverse-mode automatic differentiation algorithm[2] used to reconstruct the total phase and ultimately, calculate the magnetic induction at the nano-scale limit.

[1] A. McCray et al., Physical Review Applied 15 (2021), doi: 10.1103/PhysRevApplied.15.044025.
[2] T. Zhou et al., npj Computational Materials 7 (2021), doi: 10.1038/s41524-021-00600-x.

This work was supported by U.S. Department of Energy (DOE), Office of Science, Office of Basic Energy Sciences, Materials Sciences and Engineering Division. Use of the Center for Nanoscale Materials, an Office of Science user facility, was supported by the U.S. Department of Energy, Office of Science, Office of Basic Energy Sciences, under Contract No. DE-AC02-06CH11357.

GEOMETRIC CONFINEMENT AND PROXIMITY EFFECTS ON MAGNETIC TEXTURES IN NANOSCALE PATTERNED MAGNETIC THIN FILMS

Kayna L. Mendoza Trujillo[1,2*], Ralu Divan[2,3], Yue Li[2], Yi Jiang[2,4], Arthur R. C. McCray[2,5], Amanda K. Petford-Long[1,2], and Charudatta Phatak[1,2]

Understanding the fundamental physics and dynamic behaviour of spin textures at the atomic and nano-scale limit is critical in engineering innovative and energy efficient technologies that can be used for information storage. The aim of this project was to create arrays of magnetic islands in which this behaviour can be explored as a function of size and inter-island spacing.

NANO-SCALE FABRICATION

- Electron beam lithography (EBL) was used to pattern the top and bottom layers of resist into bars of different sizes for physical vapor deposition.
- Thin films of Cr/$Ni_{80}Fe_{20}$/Cr were deposited directly on transmission electron microscopy (TEM) silicon-nitride (SiN_x) membranes on a Si TEM chip using magnetron sputtering to reach an ideal depth of 20 nm.
- Evaporation deposition was used to directly deposit a C de-charging layer onto the TEM chip to prevent charging during imaging.
- Atomic force microscopy showed that the thickness (depth) of the larger nano-islands as depicted by line 1 in Figure 1-middle averaged 4.37 nm whereas the smallest nano-islands depicted by lines 2 and 3 averaged 4.35 nm.

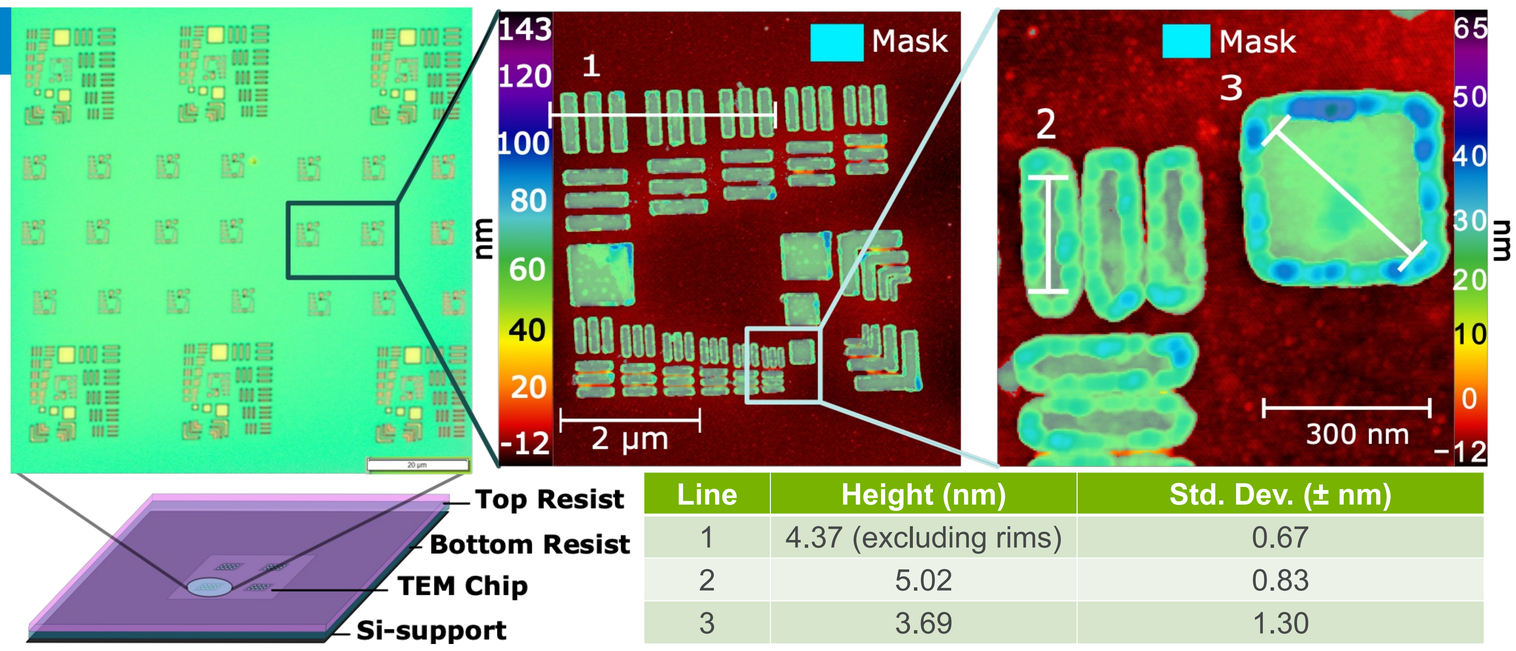

Line	Height (nm)	Std. Dev. (± nm)
1	4.37 (excluding rims)	0.67
2	5.02	0.83
3	3.69	1.30

Figure 1. (left) Schematic diagram of the EBL-prepared Si TEM chip; inset image is an optical micrograph post-magnetron sputtering deposition. (middle and right) AFM data overlayed with a blue mask; (middle) entire nano-island array, and (right) magnified inset of smallest nano-islands featuring thick remnant resist walls.

ADVANCED MICROSCOPY CHARACTERIZATION

- Aberration-corrected Lorentz TEM (ALTEM) allows direct observation of magnetic domains, film morphology, and defects in a field-free environment.

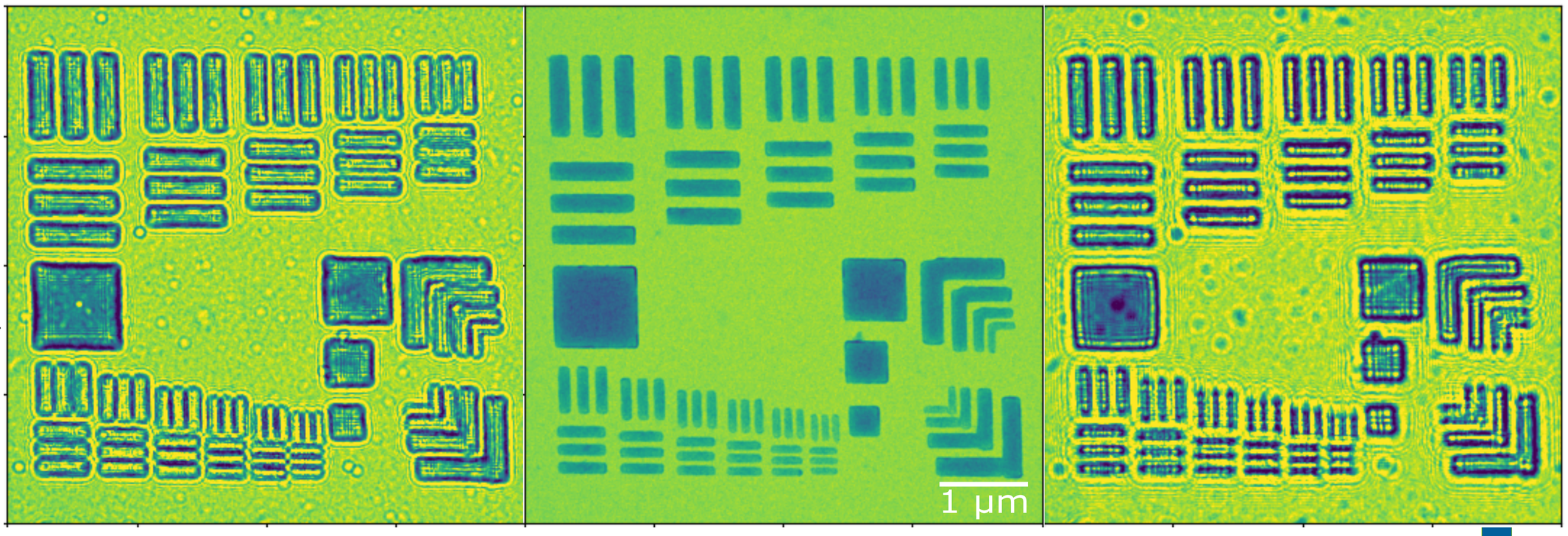

Figure 2. ALTEM through-focal-series set of nano-scale magnetic islands at various defocus conditions: (left) over focus condition, (middle) in focus condition, and (right) under focus condition.

RESULTS

- Through modification of electron dose, we successfully patterned islands with inter-island spacing as small as 17.5 nm with dimensions of 283.0 nm by 80.4 nm.
- Thickness' of nano-islands varies across the patterned array arises from remnant resist "walls" created during EBL which likely interfered with uniform deposition during magnetron sputtering deposition.
- Magnetic configurations were directly observed using ALTEM through-focal-series (TFS) imaging.
- Post-processing of ALTEM TFS micrographs enabled the total phase shift of the exiting electrons that traversed the sample to be calculated.
- Reconstruction of the magnetic induction was calculated by mapping the gradient of the phase shift which depicts the magnetic textures in the islands.

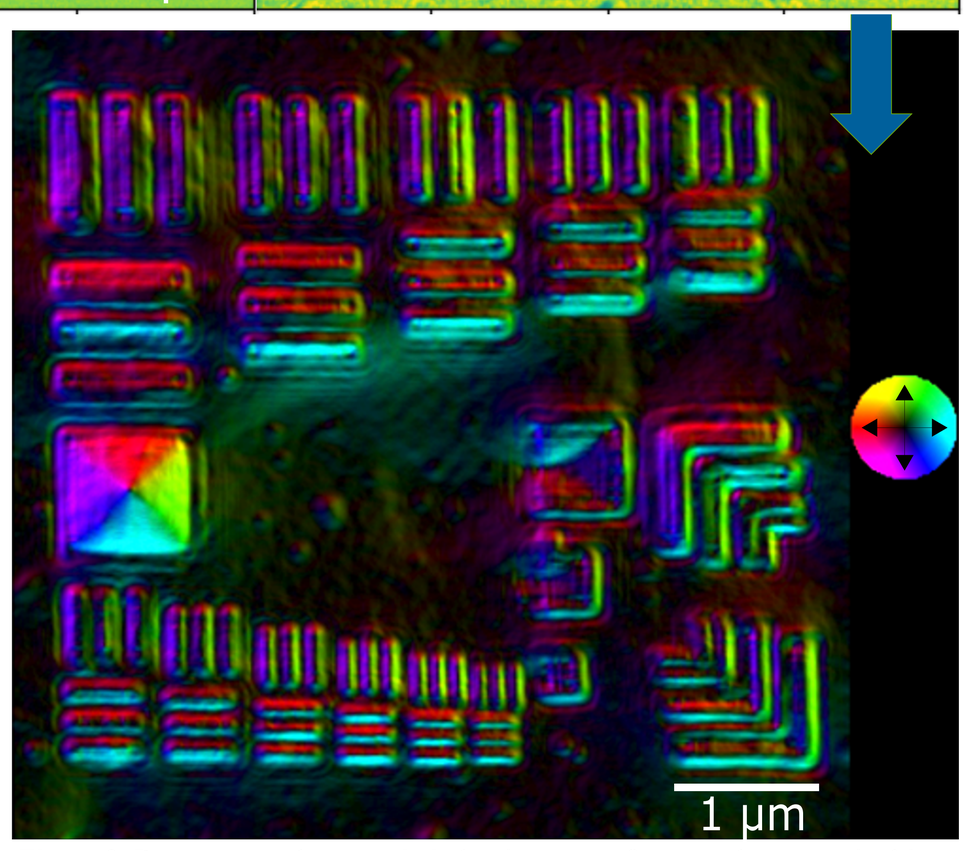

Figure 3. Reconstructed magnetic induction map of nanoscale magnetic thin film islands calculated from the gradient of the total phase shift.

FUTURE CONSIDERATIONS

- We will explore using a thinner layer of resist to reduce or potentially eliminate remnant resist walls that has a direct effect on the success of uniform physical vapor deposition of magnetic thin films.

U.S. DEPARTMENT OF ENERGY
Argonne National Laboratory is a U.S. Department of Energy laboratory managed by UChicago Argonne, LLC.

1.This work was supported by U.S. Department of Energy (DOE), Office of Science, Office of Basic Energy Sciences, Materials Sciences and Engineering Division. Use of the Center for Nanoscale Materials, an Office of Science user facility, was supported by the U.S. Department of Energy, Office of Science, Office of Basic Energy Sciences, under Contract No. DE-AC02-06CH11357.
2.Work performed at the Center for Nanoscale Materials, a U.S. Department of Energy Office of Science User Facility, was supported by the U.S. DOE, Office of Basic Energy Sciences, under Contract No. DE-AC02-06CH11357 under CNM 78451.

Argonne NATIONAL LABORATORY

LRL-CAT Post-APS-U: A High-throughput and Microfocus Protein Crystallography Beamline

Anton J. Frommelt[1], Michael Bolbat[1], Kevin L. D'Amico[1], John Koss[1], Laura L. Morisco[1], and Jordi Benach[1]

[1]LRL-CAT, Eli Lilly and Company, Advanced Photon Source, Argonne National Laboratory, Argonne, IL 60439

Eli Lilly and Company operates its own fully automated x-ray macromolecular crystallography beamline, LRL-CAT, on sector 31 of the Advanced Photon Source (APS) of Argonne National Laboratory. LRL-CAT runs exclusively as an unscheduled mail-in facility for protein crystallography, providing high quality crystallographic diffraction data for Lilly, other pharmaceutical companies, and General Users of the APS. An expert, full-time staff maintains the beamline, monitoring the automated diffraction measurements and intervening manually when needed to provide the best data from each batch of crystals. Users receive the data as soon they are collected and processed. Data collected at LRL-CAT has resulted in publications with many high-impact journals, such as *Nature*, *Journal of American Chemical Society*, and *Cell*. LRL-CAT has been preparing for the APS Upgrade for several years in order to fully utilize the new capabilities of the 4th generation light source. Recent beamline upgrades include a Kohzu cryocooled Si (111) monochromator, a Pilatus3 S 6M detector, and an ISARA unipuck sample handler robot. A new pair of Kirkpatrick-Baez focusing mirrors (JTEK/IRELEC), the highest quality that can be procured, will be installed during the APS-U. These mirrors will allow LRL-CAT to operate in two modes: 1) a high throughput mode with relatively larger beam sizes (approximately 30 x 30 to 50 x 50 μm^2 (HxV) at sample position) to facilitate fast, high-quality data collection from well-characterized projects and 2) a micro-focus mode using a 7 x 2 μm^2 (HxV) focused beam that will allow for collection on microcrystals and utilize very fine rastering and crystal cartography. This mode is aimed at tackling more challenging macromolecules. LRL-CAT looks forward to welcoming users back following the dark period with an anticipated return to operations in November of 2024.

LRL-CAT Post APS-U: A Dual-Mode Protein Crystallography Beamline

Anton J. Frommelt, Michael J. Bolbat, Kevin L. D'Amico, John W. Koss, Laura L. Morisco, Jordi Benach

LRL-CAT, Eli Lilly and Company, Advanced Photon Source, Argonne National Laboratory, Argonne, IL, 60439

Highly automated – Unscheduled – Mail-in – Auto-collection & processing – On-the-fly data transfer – Fast data turnaround – High Throughput and Micro-Focus modes

Eli Lilly and Co. operates its own fully automated X-ray macromolecular crystallography beamline, LRL-CAT, on sector 31 of the APS of Argonne National Laboratory. LRL-CAT exclusively runs as an unscheduled mail-in facility for protein crystallography, providing high quality diffraction data for Lilly, other pharmaceutical companies, and General Users of the APS. An expert, full-time staff maintains the beamline, monitoring the automated diffraction measurements and intervening manually to provide the best data from each batch of crystals. **Users can send their samples any time and receive the diffraction data as soon they are collected and processed, usually the next day.** Data collected at LRL-CAT has resulted in publications with many high-impact journals, such as *Nature*, *Journal of American Chemical Society*, and *Cell*. With the new X-ray beam from the APS-U, a new monochromator, and new focusing mirrors, two different modes of operation will be available as described below.

LRL-CAT has implemented major upgrades in preparation for the APS Upgrade:

- Kohzu cryocooled Si (111) monochromator
- Pilatus3 S 6M detector
- ISARA UniPuck sample handling robot
- JTEK / IRELEC Kirkpatrick-Baez focusing mirrors
  - Installation during APS-U
- Fluorescence detector at sample position
  - Installation during APS-U

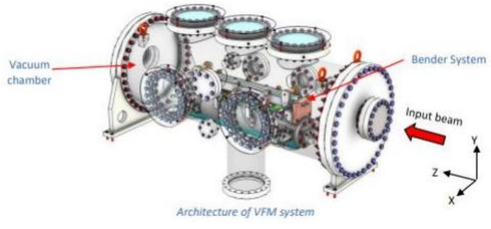

HIGH THROUGHPUT MODE

beam size range ~25x25 to 100x100 µm² (HxV)

SBDD, fragment screening, established projects

- Fast
- Improved loop and X-ray centering routines
- Improved strategy data collection routines
- Automated data processing

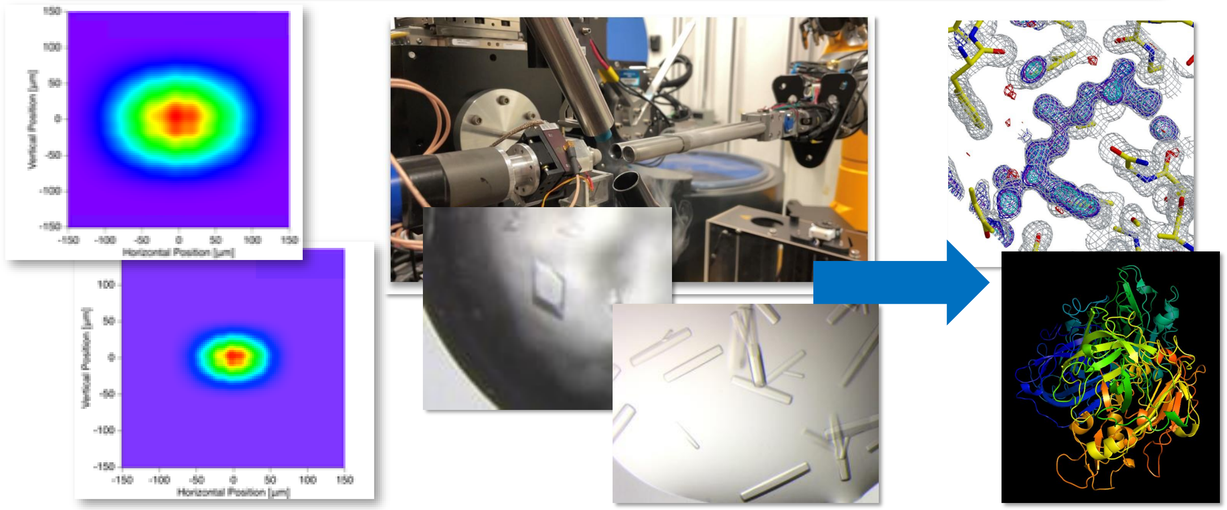

MICRO-FOCUS MODE

beam size ~7x2 µm² (HxV)

Membrane proteins, macromolecular interactions, micro-crystals

- Very fine X-ray crystal centering & cartography
- Iterative automated data collection to:
  - ✓Improve resolution, completeness, multiplicity, anomalous signal
  - ✓Achieve or improve *de novo* phasing
  - ✓Optimize macromolecule/ligand e-density maps

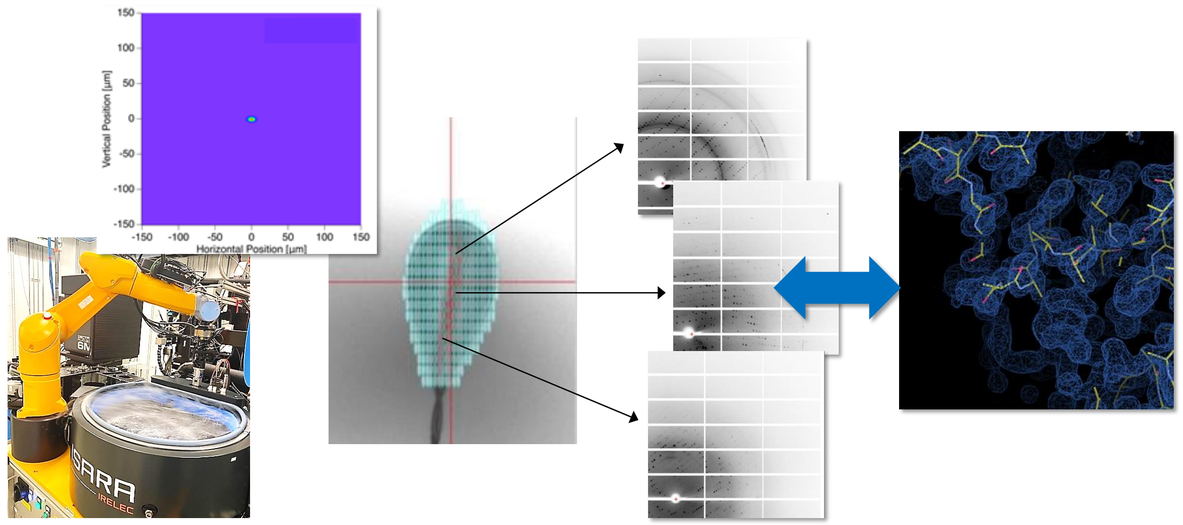

Synchrotron Powder Diffraction Simplified: The High-resolution Diffractometer 11-BM at the Advanced Photon Source

Lynn Ribaud[1] and Saul H. Lapidus[1]

[1]Advanced Photon Source, Argonne National Laboratory, Lemont, IL 60439

Synchrotrons have revolutionized powder diffraction. They enable the rapid collection of high quality powder diffraction patterns with tremendous resolution and superb signal to noise. In addition, the high penetration and exceptional data sensitivity possible at high-energy light sources, like the Advanced Photon Source (APS), allow exploration of trace containment levels, *in-situ* sample environments and crystallographic site occupancies which previously demanded neutron sources. Despite all these advantages, relatively few scientists today consider using a synchrotron for their powder diffraction studies.

To address this, the high resolution synchrotron powder diffractometer beamline 11-BM at the APS offers rapid and easy mail-in access for routine structural analyses with truly world-class quality data.[1] This instrument offers world-class resolution and sensitivity and is a free service for non-proprietary users.[2] The instrument can collect a superb pattern suitable for Rietveld analysis in less than an hour, is equipped with a robotic arm for automated sample changes, and features variable temperature sample environments. Users of the mail-in program typically receive their high-resolution data within two weeks of sample receipt. The diffractometer is also available for on-site experiments requiring more specialized measurements.

This presentation will describe this instrument, highlight its capabilities, explain the types of measurements currently available, as well as recent significant improvements to the instrument's performance. We will discuss plans to improve access and the available sample environments and collection protocols. We are particularly interested in seeking input from potential users within the powder diffraction community.

More information about the 11-BM diffractometer and its associated mail-in program can be found at our website: http://11bm.xray.aps.anl.gov.

[1] Wang, J., et al, (2008) Review of Scientific Instruments v 79, p 085105. [2] Lee, P. L., et al, (2008) Journal of Synchrotron Radiation, v 15, p 427.